

TAUP-2447-97
 Wash. U. HEP/97-61
 HU-EP-97/46
 UTCCP-P-24

August 1997

On the Phase Diagram of a Lattice U(1) Gauge Theory with Gauge Fixing

Wolfgang Bock[#], Maarten F.L. Golterman[§], Yigal Shamir[&]

Abstract

As a first step towards a nonperturbative investigation of the gauge-fixing (Rome) approach to lattice chiral gauge theories we study a U(1) model with an action that includes a local gauge-fixing term and a mass counterterm for the gauge fields. The model is studied on the trivial orbit so that only the dynamics of the longitudinal gauge degrees of freedom is taken into account. The phase diagram of this higher-derivative scalar field theory is determined, both in the mean-field approximation and numerically. The continuum limit of the model corresponds to a continuous phase transition between a ferromagnetic (FM) phase where the global U(1) symmetry is broken, and a so-called helicoidal ferromagnetic (FMD) phase with broken U(1) symmetry and a nonvanishing condensate of the vector field. The global U(1) symmetry is restored in this continuum limit. We show that our data for the magnetization in the FM and FMD phases are in good agreement with perturbation theory.

[#] Institute for Computational Physics, Humboldt University Berlin
 Invalidenstr. 110, 10099 Berlin, Germany
 e-mail: *bock@linde.physik.hu-berlin.de*

[§] Department of Physics, Washington University
 St. Louis, MO 63130, USA
 e-mail: *maarten@aapje.wustl.edu*

[&] School of Physics and Astronomy,
 Beverly and Raymond Sackler Faculty of Exact Sciences Tel-Aviv University
 Ramat Aviv 69978, Israel
 e-mail: *ftshamir@wicc.weizmann.ac.il*

1 Introduction

All existing lattice fermion formulations have in common that they are in conflict with chiral gauge invariance. It is well known that for example the Wilson-term [1], which is used to remove the 15 unwanted species doublers at the corners of the four dimensional Brillouin zone, is not invariant under chiral gauge transformations, because it has the structure of a mass term.

Most fermion formulations can be rendered gauge invariant by inserting Higgs fields. The Wilson mass term for instance turns into a Wilson-Yukawa term which is invariant under chiral gauge transformations [2, 3]. These Higgs fields do not need to be added by hand. They appear automatically in the gauge noninvariant model when performing the integration over all gauge fields in the lattice path integral with the Haar measure [4]. The Higgs fields can be identified with the longitudinal gauge degrees of freedom.

The failure of most proposals for lattice chiral gauge theories, such as the Eichten-Preskill model [5], the domain wall fermion model with waveguide [6] or the Wilson-Yukawa (Smit-Swift) model [7] is connected to the dynamics of these Higgs fields.

In the Wilson-Yukawa model, for example, it has been shown, that the 15 unwanted species doublers can indeed be removed from the spectrum by means of the Wilson-Yukawa term in the strong Wilson-Yukawa coupling symmetric phase. The model fails however because the left-handed fermion, which is the one that is supposed to couple to the gauge field, forms a fermionic bound state with the Higgs field that does not transform under the gauge group. This neutral left-handed fermion pairs up with the right-handed fermion to form a Dirac fermion which in the continuum limit decouples from the gauge field [7]. Later, arguments have been given that the spectrum in a symmetric phase is in general vector-like [8, 9].

The details of the mechanism which spoils the chiral nature of the fermions differ from model to model, but remarkably the Higgs fields (longitudinal gauge degrees of freedom) play the key role (for recent reviews see refs. [9, 10]). It is therefore natural that one should try to use gauge fixing to control the effect of these longitudinal gauge degrees of freedom [11].

Gauge fixing has been put forward some time ago as a method to discretize chiral gauge theories on the lattice [12]. It was proposed in ref. [12] to use perturbation theory in the continuum as guideline and transcribe the gauge-fixed continuum path integral to the lattice. Since the fermion part in the action breaks chiral gauge invariance, the lattice model is not invariant under BRST symmetry. The symmetry breaking terms are compensated by counterterms that have to be added to the action. In four dimensions only the counterterms with dimension smaller than or equal to four need to be considered. They should furthermore respect all exact symmetries of the lattice model. The coefficients of these terms then have to be adjusted such that BRST invariance is restored in the continuum limit. A lattice

discretization of a nonlinear gauge, $\sum_{\mu} \{\partial_{\mu} A_{\mu} + A_{\mu}^2\} = 0$, has been introduced in ref. [11], while a lattice discretization of the Lorentz gauge $\sum_{\mu} \partial_{\mu} A_{\mu} = 0$ was later given in ref. [13]. It was pointed out in ref. [11] that the lattice action of the gauge-fixing approach can be rewritten with Higgs fields and that on the trivial orbit the gauge-fixing term reduces to a higher-derivative scalar field theory. Higher-derivative scalar field theories have been studied recently in a series of papers [14], but in a very different context.

The Higgs field represents the longitudinal modes of the gauge field. The central question is then whether the fluctuations of the longitudinal modes *alias* the Higgs field are sufficiently reduced by the gauge-fixing term that the chiral nature of the fermions does not get spoiled [11]. In order to study this question, it is useful to introduce the notion of a *reduced model*. The reduced model is obtained by keeping only the Higgs fields, setting the gauge field equal to zero. (In the model without explicit Higgs field, this corresponds to restricting the gauge field to the trivial orbit.) This reduced model should then have a continuum limit with free fermions in the desired chiral representations of the gauge group.

In this paper, we will consider the reduced version of the purely bosonic model with compact U(1) symmetry that apart from the usual plaquette term includes the Lorentz gauge-fixing term of ref. [13] and a mass counterterm for the gauge field. We will derive the phase diagram of the reduced model, using mean-field and numerical techniques. We will demonstrate the existence of a continuous phase transition between a phase with broken symmetry (FM phase) and a so-called *helical ferro-magnetic* (FMD) phase, where a continuum limit can be defined. The nature of this continuum limit will be investigated using both perturbation theory and numerical simulations. In the framework of the Smit-Swift model we will demonstrate in two forthcoming publications [15, 16] that the unwanted Higgs-fermion bound states do indeed not emerge, when fermions are coupled to this model. The spectrum of this fermion-Higgs model contains only a left-handed fermion which couples to the gauge field, if we would turn it on again, and a right-handed free fermion which decouples from the gauge field in the continuum limit.

The outline of the paper is as follows: In Sect. 2 we start from the full action of the gauge-fixing (Rome) approach and reduce it step by step to the “reduced model” which will be the subject of this paper. In Sect. 3 we determine the phase diagram of the reduced model in the mean-field approximation. The magnetization is calculated in the weak coupling expansion in Sect. 4. We demonstrate that the magnetization vanishes when approaching the FM-FMD phase transition from both the FM and FMD phases. Sect. 5 deals with the results of the numerical simulation. The numerical results for the phase diagram are presented and compared with the mean-field results in Subsect. 5.1. The perturbative results for the magnetization are compared with numerical data of high precision in Subsect. 5.2. A brief summary

of our results and an outlook is given in Sect. 6.

2 The Model

In the continuum, gauge fixing is needed in order to make the integration over gauge orbits well-defined. The continuum gauge-fixed action for a chiral gauge theory can be written as

$$S_c = S_{c,G}(A_\mu^a) + S_{c,F}(A_\mu^a; \psi_L, \psi_R) + S_{c,g.f.}(A_\mu^a) + S_{c,ghost}(A_\mu^a; \bar{c}, c) . \quad (2.1)$$

Here

$$S_{c,F}(A_\mu^a; \psi_L, \psi_R) = \int d^4x \left\{ \bar{\psi}_L(x) \not{D} \psi_L(x) + \bar{\psi}_R(x) \not{\partial} \psi_R(x) \right\} \quad (2.2)$$

is the fermionic part of the action. Only the left-handed component of the fermion couples to the gauge field. $S_{c,G}(A_\mu^a)$ is the gauge action, $S_{c,g.f.}(A_\mu^a)$ the gauge-fixing action and $S_{c,ghost}(A_\mu^a; \bar{c}, c)$ is the Fadeev-Popov ghost action. For the Lorentz gauge,

$$S_{c,g.f.}(A_\mu^a) = \frac{1}{2\xi} \sum_a \left(\sum_\mu \partial_\mu A_\mu^a \right)^2 , \quad (2.3)$$

$$S_{c,ghost}(A_\mu^a; \bar{c}, c) = \sum_{a,b} \bar{c}_a \left[\delta_{a,b} \square^2 + g f_{abc} A_\mu^c \partial_\mu \right] c_b , \quad (2.4)$$

where c designates the complex ghost field, ξ is the gauge-fixing parameter, g the gauge coupling, A_μ^a the gauge field and f_{abc} are the structure constants of the gauge group. The continuum path integral is invariant under BRST transformations which replace the local gauge invariance.

The action is transcribed to the lattice using the compact lattice link variables

$$U_{\mu x} = \exp(ia g A_{\mu x}) \in G , \quad (2.5)$$

where a denotes the lattice spacing. In the following we will set a equal to one. The compact link variables are elements of the gauge group G and are assigned to the lattice links $(x, x + \hat{\mu})$. The action on the lattice can then be written in the form,

$$S = S_G(U) + S_F(U; \psi_L, \psi_R) + S_{g.f.}(U) + S_{ghost}(U; \bar{c}, c) + S_{c.t.}(U; \psi_L, \psi_R; \bar{c}, c) . \quad (2.6)$$

Only the plaquette action $S_G(U)$ is manifestly gauge invariant. To transcribe the fermion action (2.2) to the lattice one has to choose a particular lattice fermion formulation (like Wilson, domain wall or staggered fermions). All known lattice fermion formulations are in conflict with local chiral gauge invariance and, as a consequence, $S_F(U; \psi_L, \psi_R)$ is not invariant under BRST symmetry. This means that counterterms have to be added to the action so that this symmetry is restored

in the continuum limit. We have to consider all terms with dimension smaller than or equal to four, which respect all exact symmetries of the lattice model.

In this paper we will not consider fermions and focus only on the discretization of the bosonic part of the action (2.1). It turns out that also the gauge-fixing part of the action, i.e. the combination $S_{\text{g.f.}}(U) + S_{\text{ghost}}(U; \bar{c}, c)$, should be formulated on the lattice such that BRST symmetry is broken. The reason is a theorem [17] which states that the partition function itself, as well as expectation values of gauge invariant observables, vanish in a lattice model with exact BRST invariance, due to the existence of lattice Gribov copies (see also ref. [18]).

As a second simplification we choose U(1) as gauge group. This choice makes both the analytical and numerical calculations considerably easier since the ghost action in eq. (2.4) does not depend on the gauge potential and there are also no counterterms which couple the ghosts to other fields in the action. This implies that in the abelian case the ghost sector can be dropped completely from the path integral.

Finally, as a third simplification we include only the gauge-boson mass counterterm for the gauge field (this is the only counterterm of dimension two) and ignore all counterterms of higher dimension. The coefficient of this mass counterterm has to be tuned such that the photons are massless. For all dimension-four counterterms without derivatives it has been argued in ref. [13] that they do not alter the phase structure of the physically relevant region of the phase diagram (the existence of a continuous FM-FMD phase transition). We believe that this remains also true if all other counterterms are included in the action.

The U(1) model we are studying in this paper is then defined by the path integral,

$$Z = \int DU \exp(-S(U)) \quad (2.7)$$

where the action is given by

$$S(U) = S_G(U) + S_{\text{g.f.}}(U) + S_m(U) , \quad (2.8)$$

$$S_G(U) = \frac{1}{g^2} \sum_{x\mu\nu} \{1 - \text{Re } U_{\mu\nu x}\} , \quad (2.9)$$

$$S_{\text{g.f.}}(U) = \tilde{\kappa} \left\{ \sum_{x,y,z} \square(U)_{xy} \square(U)_{yz} - \sum_x B_x^2 \right\} , \quad (2.10)$$

$$S_m(U) = -\kappa \sum_{\mu x} \{U_{\mu x} + U_{\mu x}^\dagger\} . \quad (2.11)$$

Here $U_{\mu\nu x} = U_{\mu x} U_{\nu x + \hat{\mu}} U_{\mu x + \hat{\nu}}^\dagger U_{\nu x}^\dagger$ is the usual plaquette variable,

$$\square(U)_{xy} = \sum_{\mu} \{U_{\mu x} \delta_{x+\hat{\mu},y} + U_{\mu x - \hat{\mu}}^\dagger \delta_{x-\hat{\mu},y} - 2 \delta_{x,y}\} \quad (2.12)$$

is the covariant lattice laplacian,

$$B_x = \sum_{\mu} \left(\frac{V_{\mu x - \hat{\mu}} + V_{\mu x}}{2} \right)^2, \quad (2.13)$$

with

$$V_{\mu x} = \frac{1}{2i} (U_{\mu x} - U_{\mu x}^\dagger) = g A_{\mu x} + O((g A_{\mu x})^3), \quad (2.14)$$

and

$$\tilde{\kappa} = \frac{1}{2\xi g^2}. \quad (2.15)$$

The reader can easily verify that the gauge-fixing action (2.10) reduces in the classical continuum limit to eq. (2.3). The gauge-fixing term (2.3) can be transcribed to the lattice in many different ways. The choice in eq. (2.10) is motivated by the following important properties [13]:

1. The action (2.10) has a unique absolute minimum at $U_{\mu x} = 1$, validating the weak coupling expansion.
2. The action (2.10) is not BRST invariant. This is related to the fact that it cannot be written as a square of (a discretized version of) the gauge-fixing functional, $\sum_{\mu} \partial_{\mu} A_{\mu}$. The theorem of ref. [17] therefore does not apply in our case.
3. The action (2.10) leads to critical behavior in the continuum limit $g \rightarrow 0$.

In connection with item 1 we note that the naive discretization of the gauge-fixing action

$$S_{\text{g.f.}}(U) = \frac{1}{2\xi g^2} \sum_x \left(\sum_{\mu} (V_{\mu x} - V_{\mu x - \hat{\mu}}) \right)^2, \quad (2.16)$$

where eq. (2.14) was used to transcribe $A_{\mu x}$ in (2.3) in terms of $U_{\mu x}$, does not have a unique minimum. It was demonstrated in ref. [11] that this action gives rise to a dense set of lattice Gribov copies. Such a dense set of Gribov copies may still give rise to strong fluctuations of the longitudinal gauge degrees of freedom, a situation which we want to avoid from the start.

Some first information about the phase structure of the model is obtained in the constant field approximation. In this approximation the lattice link field in eq. (2.5) is replaced by a constant gauge field that is independent of x . All terms which contain derivatives of the gauge field vanish when we insert this constant gauge field into eq. (2.8) and therefore we obtain an expression for the classical potential. After expanding the resulting expression for the classical potential in powers of g we find

$$V_{\text{cl}}(A_{\mu}) = \kappa \left\{ g^2 \sum_{\mu} A_{\mu}^2 + \dots \right\} + \frac{g^4}{2\xi} \left\{ \left(\sum_{\mu} A_{\mu}^2 \right) \left(\sum_{\mu} A_{\mu}^4 \right) + \dots \right\}, \quad (2.17)$$

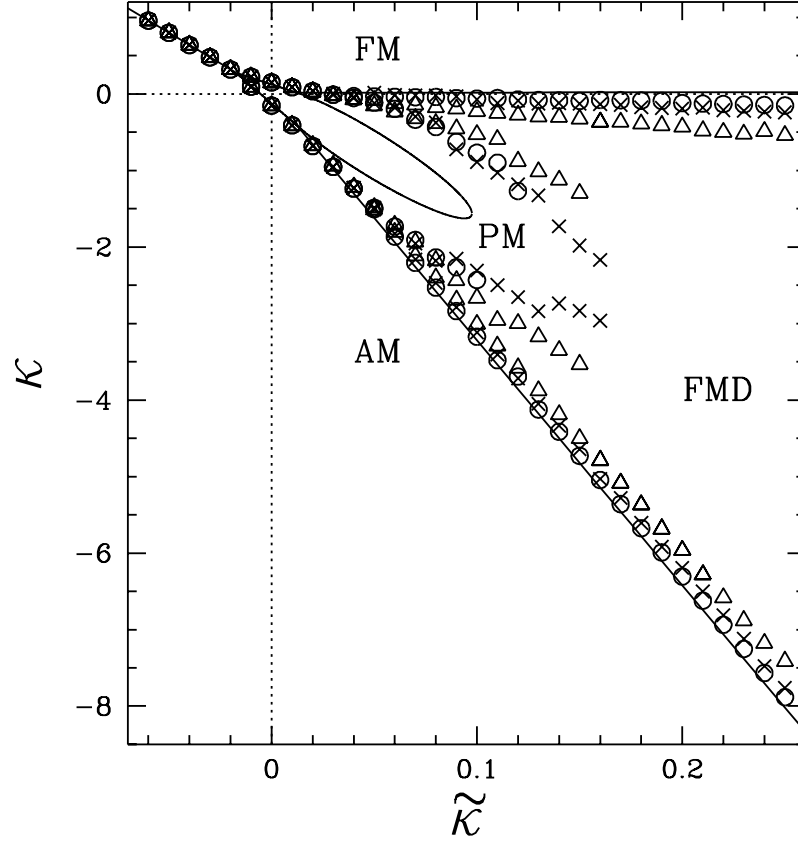


Figure 1: The $(\kappa, \tilde{\kappa})$ phase diagram of the reduced model (2.24) contains four different phases: a ferromagnetic (FM), an antiferromagnetic (AM), a paramagnetic (PM) and a directional ferromagnetic (FMD) phase. The phase boundaries in the mean-field approximation, obtained in the infinite volume limit, are represented by the solid lines. The numerical results for the phase transitions, obtained by scanning the parameter space in κ direction on the 4^4 , 6^4 and 8^4 lattices are marked by the triangles, crosses and circles. The error bars are omitted in all cases since they are smaller than the symbol size.

where the ... represent terms of higher order in g^2 . The coefficient of the term quadratic in A_μ has to be tuned such that the gauge-boson mass vanishes. The value of κ where the gauge-boson mass vanishes at a given value of g^2 defines a critical point $\kappa_{\text{FM-FMD}}(g^2)$. Using eq. (2.15) we can also replace g^2 everywhere in the series by $\tilde{\kappa}$. At tree-level we find, from eq. (2.17),

$$\kappa_{\text{FM-FMD}}(\tilde{\kappa}) = 0 , \quad (2.18)$$

which is a good approximation only in the large $\tilde{\kappa}$ region of the phase diagram. A first glance at the phase diagram in fig. 1 (which was obtained on the trivial orbit, i.e. $U_{\mu x} = g_x g_{x+\hat{\mu}}^\dagger$) shows that the mean field and numerical results for the FM-FMD phase transition at large $\tilde{\kappa}$ are indeed very close to the $\kappa = 0$ axis. We will show later that the critical coupling $\kappa_{\text{FM-FMD}}(\tilde{\kappa})$ is shifted by perturbative corrections to a small positive value.

The minimization of eq. (2.17) shows that

$$\begin{aligned} \langle g A_\mu \rangle &= 0 , & \text{for } \kappa &\geq \kappa_{\text{FM-FMD}} , \\ \langle g A_\mu \rangle &= \pm (|\kappa - \kappa_{\text{FM-FMD}}|/(6 \tilde{\kappa}))^{1/4} , & \text{for } \kappa < \kappa_{\text{FM-FMD}} , \end{aligned} \quad (2.19)$$

for all $\mu = 1, \dots, 4$ [13]. This implies that $\kappa = \kappa_{\text{FM-FMD}} = 0$ corresponds to a phase transition between a ferromagnetic (FM) phase, where $\langle A_\mu \rangle$ vanishes and the gauge boson has a nonzero mass, and a so-called FMD phase with a nonvanishing vector condensate $\langle A_\mu \rangle$. It will become clear shortly why these phases are called ferromagnetic. The abbreviation FMD stands for *ferromagnetic directional* to express the fact that the vectorial vacuum expectation value $\langle A_\mu \rangle$ induces a space-time direction and that, as a consequence, hypercubic rotation invariance is broken. The continuum limit of the model corresponds to the continuous phase transition between the FM phase and the FMD phase.

To investigate the properties of the model (2.8) beyond the constant field approximation we can study fluctuations around the classical ground state in the FM and FMD phase by expanding the observables in powers of g^2 , or alternatively powers of $1/\tilde{\kappa}$, cf. eq. (2.15).

Next we demonstrate that the model defined by the path integral (2.7) is equivalent to a gauge-Higgs model which is manifestly gauge invariant. The lattice path integral in (2.7) can be rewritten as [4]

$$\begin{aligned} Z &= \int DU \exp(-S(U_{\mu x})) \\ &= \int DU \exp(-S(g_x U_{\mu x} g_{x+\hat{\mu}}^\dagger)) \\ &= \int DU D\phi \exp(-S(\phi_x^\dagger U_{\mu x} \phi_{x+\hat{\mu}})) \end{aligned} \quad (2.20)$$

where in the second line we have performed a local gauge transformation, $U_{\mu x} \rightarrow g_x U_{\mu x} g_{x+\hat{\mu}}^\dagger$, $g_x \in G$ and made use of the gauge invariance of the Haar measure. The g_x 's drop out of the plaquette action because it is manifestly gauge invariant. The third line is obtained after integrating both sides of the equation (2.20) over the gauge degrees of freedom with $g_x = \phi_x^\dagger$ and using the fact that $\int D\phi = 1$. This simple transformation shows that the longitudinal gauge degrees of freedom turn into group-valued Higgs fields. The new action $S(\phi_x^\dagger U_{\mu x} \phi_{x+\hat{\mu}})$ is now invariant under the gauge transformations

$$U_{\mu x} \rightarrow h_x U_{\mu x} h_{x+\hat{\mu}}^\dagger, \quad \phi_x \rightarrow h_x \phi_x. \quad (2.21)$$

We will refer in the following to $S_V = S(U_{\mu x})$ in eq. (2.8) as the action in the *vector* picture and to $S_H = S(\phi_x^\dagger U_{\mu x} \phi_{x+\hat{\mu}})$ in eq. (2.20) as the action in the *Higgs* picture. The two actions are related by

$$S_V(U_{\mu x}) = S_H(U_{\mu x}; \phi_x)|_{\phi=1} \quad (2.22)$$

and all observables in the vector picture are mapped onto corresponding observables in the Higgs picture (see also ref. [11]).

In this paper we will study a *reduced* model defined by the action (2.8) on the trivial orbit, $U_{\mu x} = g_x \mathbb{1} g_{x+\hat{\mu}}^\dagger$. In the Higgs picture, cf. eq. (2.20), the reduced model is obtained by setting $U_{\mu x} = 1$. The reduced model is then defined by the following lattice path integral

$$Z = \int D\phi \exp(-S(\phi)) \quad (2.23)$$

$$S(\phi) = -\kappa \sum_x \phi_x^\dagger (\square \phi)_x + \tilde{\kappa} \sum_x \left\{ \phi_x^\dagger (\square^2 \phi)_x - B_x^2 \right\}, \quad (2.24)$$

where B_x is given by eq. (2.13) with

$$V_{\mu x} = \frac{1}{2i} \left(\phi_x^\dagger \phi_{x+\hat{\mu}} - \phi_{x+\hat{\mu}}^\dagger \phi_x \right). \quad (2.25)$$

Eq. (2.24) defines a higher-derivative scalar field theory.

As a first step we will investigate in the following the phase diagram of the reduced model. Eq. (2.24) shows that the partition function is invariant under the symmetry

$$\kappa \rightarrow -\kappa - 32 \tilde{\kappa}, \quad \tilde{\kappa} \rightarrow \tilde{\kappa}, \quad \phi_x \rightarrow \epsilon_x \phi_x, \quad (2.26)$$

where

$$\epsilon_x = (-1)^{\Sigma(x)}, \quad \Sigma(x) = \sum_\mu x_\mu. \quad (2.27)$$

This implies that the phase diagram is symmetric under reflection with respect to the line

$$\kappa + 16 \tilde{\kappa} = 0 . \quad (2.28)$$

For $\tilde{\kappa} = 0$ we recover the XY model in four dimensions whose phase diagram consists of three different phases: a broken or ferromagnetic (FM) phase at $\kappa > \kappa_{\text{FM-PM}} > 0$, a symmetric or paramagnetic (PM) phase at $\kappa_{\text{PM-AM}} < \kappa < \kappa_{\text{FM-PM}}$ and an antiferromagnetic (AM) phase at $\kappa < \kappa_{\text{PM-AM}} < 0$. The symmetry (2.26) implies that, $\kappa_{\text{PM-AM}} = -\kappa_{\text{FM-PM}}$. Numerically it has been found that $\kappa_{\text{FM-PM}} \approx 0.15$. The order parameters which allow us to distinguish between these phases are the magnetization

$$v = |\langle \phi_x \rangle| \quad (2.29)$$

and the staggered magnetization

$$v_{\text{AM}} = |\langle \epsilon_x \phi_x \rangle| . \quad (2.30)$$

Both quantities are not invariant under the global U(1) symmetry, and we have taken the modulus to eliminate the ambiguity due to the constant field mode. The FM phase is characterized by $v > 0$, $v_{\text{AM}} = 0$, whereas in the AM phase $v = 0$, $v_{\text{AM}} > 0$. Both order parameters vanish in the intermediate PM phase.

As explained above, at large $\tilde{\kappa}$ we expect to find a new phase transition between the FM and the FMD phase, which at tree level is given by eq. (2.18). (In the following we will retain the name FMD also for the reduced-model version of the FMD phase.) The FMD phase is characterized by a new vector order parameter q_μ , $0 < q_\mu < 2\pi$, which is nonzero in the FMD phase and vanishes in the FM phase. It is equal to (π, π, π, π) in the AM phase. As a generalization of v and v_{AM} we define a helicoidal magnetization

$$v_{\text{H}} = \left| \left\langle \phi_x \exp \left(-i \sum_{\mu} q_{\mu} x_{\mu} \right) \right\rangle \right| , \quad (2.31)$$

which is nonzero in the FMD phase. It is easy to see that v_{H} reduces to v in the FM and to v_{AM} in AM phase.

When ignoring fluctuations around the ground state, the vector field $V_{\mu x}$, cf. eqs. (2.14) and (2.25), in the FMD phase is given by

$$V_{\mu x} = v_{\text{H}}^2 q_{\mu} + O(q_{\mu}^3) , \quad (2.32)$$

showing that q_{μ} plays the role of the vector condensate in the reduced model. We mention in passing that phases with nonvanishing q_{μ} have been intensively investigated in lower dimensions in condensed matter physics and are known as helicoidal-ferromagnetic phases (see ref. [19] for a recent review).

To further substantiate the statements about the phase diagram made in this section we will determine in the next section the phase diagram of the reduced model (2.24) in the mean-field approximation. Numerical data for the phase diagram are presented in Sect. 5.1 and compared with the mean-field results.

3 The Phase Diagram in the Mean-Field Approximation

In the following we will perform a mean-field analysis of the phase diagram in d dimensions.

A central problem of the mean-field approximation in more complicated ferromagnetic systems is the choice of the mean-field ansatz which in a given region of the parameter space leads to the absolute minimum of the free energy. Usually there exist many different choices and it is not straightforward to pick an ansatz which leads to the absolute minimum of the free energy. Based on the discussion of the previous section we decided to consider the ansatz

$$\phi_x = \varphi \exp \left(i \sum_{\mu} q_{\mu} x_{\mu} \right) , \quad (3.1)$$

where q_{μ} , $0 \leq q_{\mu} < 2\pi$ are real phases and φ plays the role of a magnetization. Depending on the value of q_{μ} this ansatz can distinguish between phases with ferromagnetic ($q_{\mu} = 0$, $\mu = 1, \dots, d$), $\varphi = v$, antiferromagnetic ($q_{\mu} = \pi$, $\mu = 1, \dots, d$) ordering, $\varphi = v_{\text{AM}}$, and phases with a helicoidal magnetization ($q_{\mu} \neq 0, \pi$, for at least one component μ), $\varphi = v_{\text{H}}$. Similarly, we take for the magnetic field h_x the ansatz

$$h_x = h \exp \left(i \sum_{\mu} q_{\mu} x_{\mu} \right) , \quad (3.2)$$

where h is the mean-field magnetic field.

Using eqs. (3.1) and (3.2) and following the steps of the standard mean-field calculation (see for example ref. [20]), we obtain for the free energy of the reduced model (2.24)

$$\mathcal{F}(\varphi, h, q; \tilde{\kappa}, \kappa) = L^d \left\{ 2 \varphi h - \log I_0(2h) + \sum_{i=1}^4 \varphi^{2i} f^{(i)}(q; \tilde{\kappa}, \kappa) \right\} , \quad (3.3)$$

where L is the extent of the lattice in spatial and temporal directions,

$$f^{(1)}(q; \tilde{\kappa}, \kappa) = -2 (4 d \tilde{\kappa} + \kappa) F(q) + 2 \tilde{\kappa} (2F(q)^2 - d) + \frac{\tilde{\kappa}}{16} F(2q) (2d + 1) , \quad (3.4)$$

$$f^{(2)}(q; \tilde{\kappa}, \kappa) = -\frac{\tilde{\kappa}}{64} \left(6 F(2q)^2 - 4 (3d + 1) F(2q) + d (10d - 1) \right) , \quad (3.5)$$

$$f^{(3)}(q; \tilde{\kappa}, \kappa) = -\frac{\tilde{\kappa}}{16} \left(2 F(2q)^2 - 2 (d - 1) F(2q) - d \right) , \quad (3.6)$$

$$f^{(4)}(q; \tilde{\kappa}, \kappa) = -\frac{\tilde{\kappa}}{32} (F(2q) - d)^2 , \quad (3.7)$$

$$F(q) = \sum_{\mu} \cos q_{\mu} \quad (3.8)$$

and

$$I_0(h) = \frac{1}{\pi} \int_0^{\pi} d\alpha \exp(\pm h \cos \alpha) \quad (3.9)$$

is the modified Bessel function of zeroth order. We have dropped in eq. (3.3) all terms that depend neither on φ nor on q . The saddle-point equations read

$$\frac{\partial \mathcal{F}}{\partial \varphi} = L^d \left\{ 2h + \sum_{i=1}^4 \varphi^{2i-1} 2i f^{(i)}(q; \tilde{\kappa}, \kappa) \right\} = 0 , \quad (3.10)$$

$$\frac{\partial \mathcal{F}}{\partial q_{\mu}} = L^d \varphi^2 \sin q_{\mu} \left\{ \sum_{i=1}^4 \varphi^{2i-2} g_{\mu}^{(i)}(q; \tilde{\kappa}, \kappa) \right\} = 0 , \quad (3.11)$$

$$\frac{\partial \mathcal{F}}{\partial h} = 2 L^d \left\{ \varphi - \frac{I_1(2h)}{I_0(2h)} \right\} = 0 , \quad (3.12)$$

where

$$g_{\mu}^{(1)}(q; \tilde{\kappa}, \kappa) = 2 (4d \tilde{\kappa} + \kappa) - 8 \tilde{\kappa} F(q) - \frac{\tilde{\kappa}}{4} (2d + 1) \cos q_{\mu} \quad (3.13)$$

$$g_{\mu}^{(2)}(q; \tilde{\kappa}, \kappa) = \frac{\tilde{\kappa}}{16} (12 F(2q) - 12d - 4) \cos q_{\mu} \quad (3.14)$$

$$g_{\mu}^{(3)}(q; \tilde{\kappa}, \kappa) = \tilde{\kappa} (F(2q) - \frac{1}{2} (d - 1)) \cos q_{\mu} \quad (3.15)$$

$$g_{\mu}^{(4)}(q; \tilde{\kappa}, \kappa) = \frac{\tilde{\kappa}}{4} (F(2q) - d) \cos q_{\mu} , \quad (3.16)$$

and

$$I_1(h) = \frac{dI_0(h)}{dh} \quad (3.17)$$

is the modified Bessel function of first order.

From these $d + 2$ equations we can compute the $d + 2$ fields φ , q_{μ} and h as functions of the parameters $\tilde{\kappa}$ and κ . The phase boundaries are defined as the lines in the $(\tilde{\kappa}, \kappa)$ parameter space where various combinations of the order parameters φ and q_{μ} vanish.

The variable h can be eliminated from the saddle-point equations in regions where φ is very small (which is the case close to the PM phase, where φ vanishes) and the ratio $I_1(2h)/I_0(2h)$ in eq. (3.12) can be expanded in powers of h , $I_1(2h)/I_0(2h) = h + O(h^3)$.

Usually there does not exist a unique solution of the saddle-point equations in a certain region of the parameter space. It is therefore important to substitute the various solutions back into the expression for the free energy (3.3) and to pick out the solution that corresponds to the absolute minimum. In practice it can happen that certain phases remain undetected because the mean-field ansatz was too simple. In the following we will consider also another ansatz to search for a ferrimagnetic (FI) phase in a certain region of the parameter space which cannot be probed with the ansatz (3.1). Because of this uncertainty of the mean-field calculation it is important to determine the phase diagram also numerically.

We furthermore note that the free energy in eq. (3.3) is invariant under the symmetry (2.26),

$$q_\mu \rightarrow \pi - q_\mu, \quad \kappa \rightarrow -\kappa - 8d\tilde{\kappa}, \quad \tilde{\kappa} \rightarrow \tilde{\kappa}, \quad (3.18)$$

which implies that also the phase diagram in the mean-field approximation is symmetric (but for the interchange $q_\mu \leftrightarrow \pi - q_\mu$, which maps the FM onto the AM phase, etc.) with respect to the line $\kappa + 4d\tilde{\kappa} = 0$ which in four dimensions turns into eq. (2.28).

In the following paragraph we present our mean-field results for the phase boundaries and briefly explain how they were obtained:

- **FM-PM and PM-AM transitions:** The transition between the FM and PM (PM and AM) phases is obtained by approaching the transitions from within the FM (AM) phase where $F(q) = d$, $F(2q) = d$ ($F(q) = -d$, $F(2q) = d$) and $\varphi = v$ ($\varphi = v_{\text{AM}}$) approaches zero. The relation for the FM-PM (PM-AM) phase boundary is obtained by expanding eq. (3.10) in powers of φ and equating the part that is linear in φ with zero. Eq. (3.11) is trivially fulfilled because $\sin q_\mu = 0$ in the FM (AM) phases. The FM-PM and PM-AM phase boundaries are respectively given by the relations,

$$\kappa_{\text{FM-PM}} = \frac{1}{2d} - (2d+1) \frac{31}{32} \tilde{\kappa}, \quad (3.19)$$

$$\kappa_{\text{PM-AM}} = -\frac{1}{2d} - \left(\frac{194}{32}d - \frac{31}{32} \right) \tilde{\kappa}. \quad (3.20)$$

The reader can easily verify that the two solutions are related to each other by the transformation (3.18). The FM-PM and PM-AM phase transition lines intersect at $\tilde{\kappa} = \tilde{\kappa}_1 = \left[d \left(\frac{31}{16} - \frac{33}{8}d \right) \right]^{-1}$. The corresponding solution of the

saddle-point equations minimizes the free energy (3.3) only in the interval

$$\tilde{\kappa}_1 \leq \tilde{\kappa} \leq \frac{16}{35} [d(2d+1)]^{-1} = \tilde{\kappa}_2, \quad (3.21)$$

and the two straight lines (3.19) and (3.20) therefore form the boundary of the PM phase only in that interval.

- **FMD-PM transition:** The magnetization $\varphi = v_H$ vanishes when we approach the phase boundary from the FMD side which means that eqs. (3.10) and (3.11) can be expanded in powers of φ . Unlike in the previous case $\sin q_\mu \neq 0$ for at least one component $\mu = 1, \dots, d$ and hence $-d < F(q) < +d$. From the term in eq. (3.10) that is proportional to φ we obtain

$$2(4d\tilde{\kappa} + \kappa)F(q) - 2\tilde{\kappa}(2F(q)^2 - d) - \frac{\tilde{\kappa}}{16}F(2q)(2d+1) = 1. \quad (3.22)$$

After summing the $i = 1$ term inside the curly brackets in eq. (3.11) over μ we obtain for $F(q)$ the formula

$$F(q) = 8d \frac{4d\tilde{\kappa} + \kappa}{(34d+1)\tilde{\kappa}}, \quad (3.23)$$

and after first multiplying the same term with $\cos q_\mu$ and then summing over μ we obtain an expression for $F(2q)$,

$$\frac{\tilde{\kappa}}{16}(2d+1)F(2q) = (4d\tilde{\kappa} + \kappa)F(q) - 4\tilde{\kappa}F(q)^2 - \frac{\tilde{\kappa}}{16}(2d+1)d. \quad (3.24)$$

After substituting these two solutions into eq. (3.22) and after a few trivial algebraic manipulations we obtain the following solution for the FMD-PM phase transition:

$$\kappa_{\text{FMD-PM}} = -4d\tilde{\kappa} \pm \sqrt{\frac{\tilde{\kappa}}{8d} \left[1 - \frac{\tilde{\kappa}}{16}d(2d+33) \right] (34d+1)}. \quad (3.25)$$

This solution describes an ellipse located around the symmetry axis, $\kappa + 4d\tilde{\kappa} = 0$. Eq. (3.25) forms the boundary of the PM phase in the interval

$$\tilde{\kappa}_2 \leq \tilde{\kappa} \leq 16[d(2d+33)]^{-1} = \tilde{\kappa}_3, \quad (3.26)$$

as the corresponding mean-field solution does not lead to an absolute minimum of the free energy (3.3) in the region where $\tilde{\kappa} \leq \tilde{\kappa}_2$.

- **FM-AM phase transition:** Above we pointed out that the FM-PM and PM-AM phase transitions intersect at $\tilde{\kappa} = \tilde{\kappa}_1$. This means that the FM and AM meet at this value of $\tilde{\kappa}$. Two different scenarios are imaginable for the phase structure in the region $\tilde{\kappa} < \tilde{\kappa}_1$: 1) The FM and AM phases meet at the $4d\tilde{\kappa} + \kappa = 0$ symmetry line with the magnetizations v and v_{AM} exhibiting a jump at this line, or 2) the FM and AM phases are separated by a FI phase in which both order parameters v and v_{AM} are simultaneously nonzero. The mean-field ansatz (3.1) is not suited to detect such an intermediate FI phase since q_μ cannot be equal to 0 and π at the same time. We therefore calculated the free energy also for the ansatz of the form

$$\phi_x = v + v_{\text{AM}} \epsilon_x , \quad (3.27)$$

which allows us to probe for a FI phase. Our calculation however shows that scenario 2) leads to a larger value of the free energy. Also our numerical data in four dimensions give clear evidence for the correctness of the first scenario.

- **FM-FMD and FMD-AM transitions:** The FM-FMD (FMD-AM) phase transition is characterized by $q_\mu \rightarrow 0$ ($q_\mu \rightarrow \pi$) for all $\mu = 1, \dots, d$. It is difficult to determine the location of these phase transitions analytically because φ does not vanish at these two phase transitions and eqs. (3.10)-(3.12) cannot be expanded in φ . We will show in the next section that the magnetization actually vanishes at the FM-FMD (FMD-AM) phase transition. This phenomenon is connected to the infra-red behavior of the higher-derivative action and therefore cannot be understood in the framework of the mean-field approximation.

The FM-FMD phase transition is determined by eliminating the fields h and φ from equation (3.12) and

$$\begin{aligned} & -4d\kappa - 4d\tilde{\kappa}(2d+1) + \frac{\tilde{\kappa}}{8}d(2d+1) + \frac{1}{16}\tilde{\kappa}d(-4d+5)\varphi^2 \\ & - \frac{3}{8}\tilde{\kappa}d\varphi^4 + 2\frac{h}{\varphi} = 0 , \end{aligned} \quad (3.28)$$

$$2\kappa - \frac{\tilde{\kappa}}{4}(2d+1) - \frac{1}{4}\tilde{\kappa}\varphi^2 + \frac{\tilde{\kappa}}{2}(d+1)\varphi^4 = 0 . \quad (3.29)$$

Eqs. (3.28) and (3.29) are obtained from eqs. (3.10) and (3.11) in the limit $q \rightarrow 0$. Note that eqs. (3.12), (3.28) and (3.29) can only hold simultaneously on the FM-FMD transition curve, where $F(q) = F(2q) = d$. The location of the FM-FMD transition can be calculated analytically in two special cases: at the PM-phase boundary, the terms in eq. (3.29) which are quadratic and

quartic in φ can be ignored, and the FM-FMD transition is given by the intersection of the PM-phase boundary and the line

$$\kappa_{\text{FM-FMD}} = \frac{\tilde{\kappa}}{8} (2d + 1) . \quad (3.30)$$

Similarly the FMD-AM phase transition is given by the intersection of the PM-phase boundary and the line

$$\kappa_{\text{FMD-AM}} = -8d\tilde{\kappa} - \frac{\tilde{\kappa}}{8} (2d + 1) . \quad (3.31)$$

The FM-FMD phase transition can also be calculated analytically in the limit $\tilde{\kappa} \rightarrow \infty$. Eq. (3.28) implies that $h = \tilde{\kappa}d(128d + 63)/32 + O(1)$ for $\tilde{\kappa} \rightarrow \infty$, and the expansion of φ , cf. eq. (3.12), gives $\varphi = 1 - 1/(4h) + O(1/h^2)$. After substituting these two formulas into eq. (3.29) we find

$$\kappa_{\text{FM-FMD}} \rightarrow \frac{2(4d + 3)}{(128d + 63)d} , \quad \tilde{\kappa} \rightarrow \infty . \quad (3.32)$$

In four dimensions we have determined $\kappa_{\text{FM-FMD}}(\tilde{\kappa})$ also at a series of intermediate $\tilde{\kappa}$ values by solving eqs. (3.12), (3.28) and (3.29) numerically. The results for $\kappa_{\text{FM-FMD}}(\tilde{\kappa})$ are listed (with an accuracy of four decimal places) in the second column of table 1. We have also included the mean-field value of φ evaluated at $\kappa = \kappa_{\text{FM-FMD}}(\tilde{\kappa})$ (third column). The corresponding numerical values of the FMD-AM phase transition can be easily obtained from the data in the second column of table 1 by making use of the symmetry (3.18).

The mean-field phase diagram for $d = 4$ is displayed in fig. 1. The phase boundaries are represented in this plot by the solid lines. The FM-FMD phase transition line was computed by solving eqs. (3.12), (3.28) and (3.29) numerically. The FMD-AM transition was computed from the the FM-FMD phase transition data by making use of the symmetry (3.18). The various symbols in fig. 1 represent the results of the numerical simulation and will be explained later.

4 Weak Coupling Expansion

Eq. (2.15) suggests that the weak coupling expansion should be performed in $1/\tilde{\kappa}$. We consider small fluctuations of the ϕ fields around the classical ground state, which we parametrize by the Goldstone field θ_x :

$$\phi_x = \exp \left(i \sum_{\mu} q_{\mu} x_{\mu} + i \theta_x / \sqrt{2\tilde{\kappa}} \right) . \quad (4.1)$$

	mean-field approximation	
$\tilde{\kappa}$	$\kappa_{\text{FM-FMD}}$	φ
0.013	0.01467	0.21887
0.014	0.01566	0.42089
0.015	0.01597	0.52455
0.020	0.01639	0.73962
0.025	0.01621	0.81831
0.030	0.01609	0.85916
0.050	0.01608	0.92369
0.1	0.01626	0.96377
1	0.01649	0.99651
10	0.01651	0.99965
100	0.01651	0.99997
∞	0.01652	1.00000

Table 1: The mean-field results for the critical coupling $\kappa_{\text{FM-FMD}}(\tilde{\kappa})$ and the order parameter φ evaluated at $\kappa = \kappa_{\text{FM-FMD}}(\tilde{\kappa})$ are given in columns two and three for several values of $\tilde{\kappa}$. The value of $\kappa_{\text{FM-FMD}}$ at $\tilde{\kappa} = \infty$ was calculated from eq. (3.32).

This ansatz holds both in the FM phase, where $q_\mu = 0$ and also the FMD phase, where $q_\mu \neq 0, \pi$ for at least one component $\mu = 1, \dots, 4$. The phases q_μ in the FMD phase can be computed by minimizing the effective potential, or alternatively could be taken from the numerical simulation.

To calculate v in perturbation theory, we first insert eq. (4.1) into the action (2.24) of the reduced model and expand it in powers of θ_x ,

$$S = \frac{1}{2} \int_k \theta(-k) \Delta_q^{-1}(k) \theta(k) + \int_{k_1, k_2, k_3, k_4} \mathcal{V}_q(k_1, k_2, k_3, k_4) \theta(k_1) \theta(k_2) \theta(k_3) \theta(k_4) + \dots, \quad (4.2)$$

where

$$\int_k = \int_0^{2\pi} \frac{d^4 k}{(2\pi)^4}. \quad (4.3)$$

The subscript q indicates that the propagator $\Delta_q(k)$ and four-point vertex function $\mathcal{V}_q(k_1, k_2, k_3, k_4)$ depend on the phases q_μ . The inverse propagator $\Delta_q^{-1}(k)$ is given by

$$\begin{aligned} \Delta_q^{-1}(k) = & \left\{ \sum_\mu \cos q_\mu \, 2(1 - \cos k_\mu) \right\}^2 - 8(F(q) - 4) \sum_\mu \cos q_\mu (1 - \cos k_\mu) \\ & + \left\{ 2 \sum_\mu \sin q_\mu \sin k_\mu \right\}^2 + 4 \sum_{\mu\nu} \sin^2 q_\mu \sin^2 q_\nu (1 - \cos k_\nu) \\ & - \left\{ \sum_\mu \sin 2q_\mu \sin k_\mu \right\}^2 - 2 \sum_{\mu\nu} \sin^2 q_\nu \cos^2 q_\mu \sin^2 k_\mu \\ & + m^2 \sum_\mu \cos q_\mu \, 2(1 - \cos k_\mu), \end{aligned} \quad (4.4)$$

with

$$m^2 = \frac{\kappa}{\tilde{\kappa}}. \quad (4.5)$$

(The expression for the propagator simplifies if q is a solution of the classical saddle-point equations, cf. eq. (4.13) below. As we will discuss below, however, this is not in general the case in finite volume.) At tree-level, the FM-FMD phase transition line is given by $m^2 = 0$, cf. eq. (2.18). When approaching the FM-FMD phase transition line, eq. (4.4) reduces to

$$\Delta_q(k) \propto 1/(k^2)^2, \quad \kappa \rightarrow \kappa_{\text{FM-FMD}} \quad (4.6)$$

for small k . The propagator (4.6) leads to infra-red divergences. A similar situation is encountered in two space-time dimensions where infra-red divergences occur for

massless bosons with an ordinary kinetic term [21]. These infra-red divergences are not only an artifact of the tree-level propagator, but occur in the full theory when the continuum limit $\kappa \rightarrow \kappa_{\text{FM-FMD}}$ is performed. The qualitative agreement with the two-dimensional behavior will be demonstrated below both analytically and numerically. Here we note that the situation we encounter in the reduced model is similar to the situation of the XY model in two dimensions. The FM-FMD phase transition line behaves like the spin-wave phase, where critical exponents depend continuously on the coupling constant. Below we will show that the magnetization v (helical magnetization v_{H}) vanishes $\propto |\kappa - \kappa_{\text{FM-FMD}}|^{\eta(\tilde{\kappa})}$ when $\kappa \searrow \kappa_{\text{FM-FMD}}$ ($\kappa \nearrow \kappa_{\text{FM-FMD}}$) and that the critical exponent $\eta(\tilde{\kappa})$ depends continuously on $\tilde{\kappa}$.

It is useful to distinguish between observables which are invariant under the global U(1) symmetry (symmetric), like the two-point function $\langle \phi_x^\dagger \phi_y \rangle$, and others which are not invariant (nonsymmetric), like the magnetization $\langle \phi_x \rangle$. For symmetric observables, the weak coupling expansion is infra-red finite, because all interactions involve derivatives. The situation is different for nonsymmetric observables, such as the magnetization. The real expansion parameter is not $1/\tilde{\kappa}$ in this case, but $(\log m^2)/\tilde{\kappa}$. This means that in order to obtain a nondivergent result in the limit $m^2 \rightarrow 0$, one should perform a resummation of infinitely many diagrams.

Using eqs. (4.1) and (4.2) the magnetization, cf. eq. (2.31), can be calculated to one-loop in perturbation theory,

$$v_{\text{H}} = 1 - \frac{1}{4\tilde{\kappa}} \int_k \Delta_q(k) + \text{higher order corrections} . \quad (4.7)$$

The integral in eq. (4.7) is infra-red divergent in the limit $m^2 \rightarrow 0$ and, as mentioned in the previous paragraph, in order to obtain a finite result we have to resum the higher order diagrams (with two and more lines) in fig. 2a which arise from the terms proportional to θ_x^{2n} in eq. (4.1) with $n > 1$. This resummation of diagrams gives

$$v_{\text{H}} = \exp \left(-\frac{1}{4\tilde{\kappa}} \int_k \Delta_q(k) \right) + \text{higher order corrections} \quad (4.8)$$

$$\sim \left(\frac{|\kappa|}{\tilde{\kappa}} \right)^\eta + \text{higher order corrections} , \quad (4.9)$$

where we used that at tree-level $\kappa_{\text{FM-FMD}} = 0$. The higher order corrections in eqs. (4.8) and (4.9) are due to quartic and higher order interactions which we have ignored. The critical exponent η in eq. (4.9) is given by

$$\eta = \frac{1}{64\pi^2\tilde{\kappa}} . \quad (4.10)$$

Eq. (4.9) shows that the magnetization vanishes at the FM-FMD phase transition with a critical exponent η that depends on $\tilde{\kappa}$ and differs from the Gaussian exponent

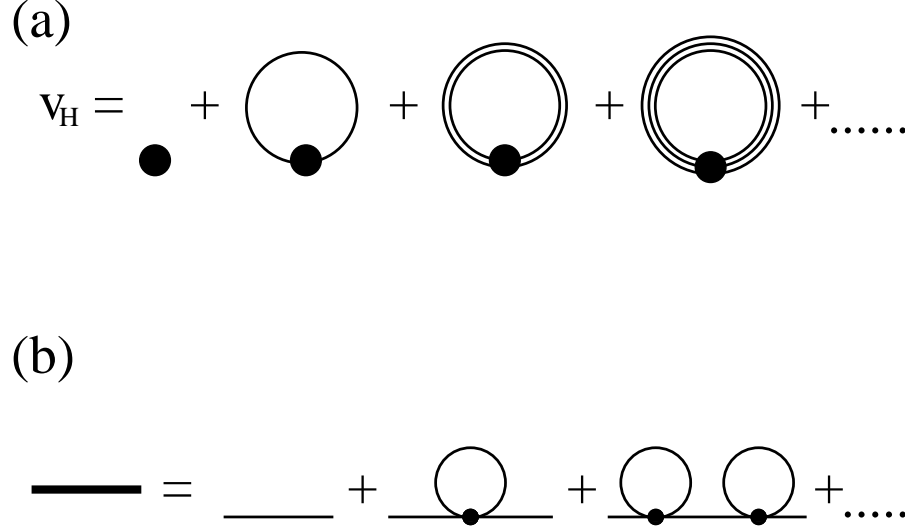


Figure 2: *Feynman diagrams for the magnetization (a) and the scalar field propagator (b).*

1/2 of the XY model at $\tilde{\kappa} = 0$. (In order to show that also the helicoidal magnetization v_H vanishes for $\kappa \nearrow \kappa_{\text{FM-FMD}}$ with the critical exponent (4.10), one uses eq. (4.4) where q is the nontrivial solution of eq. (4.13) below.)

Using relation (4.8) and replacing the integral by a lattice sum, we can compute v_H on a finite volume at any value of $\tilde{\kappa}$ and κ in the FM and FMD phases provided that we know the function $q = q(\tilde{\kappa}, \kappa)$. On a finite lattice with periodic boundary conditions for the scalar fields the phases q_μ can only take the values

$$q_\mu = 2n_\mu\pi/L, \quad n_\mu = 0, \dots, L-1, \quad (4.11)$$

where L designates the extent of the lattice in temporal and spatial directions. The q 's can be calculated at tree level by minimizing the classical action

$$S_0(q; \tilde{\kappa}, \kappa) = L^4 \left\{ -2(16\tilde{\kappa} + \kappa) F(q) + 4\tilde{\kappa} F(q)^2 - \tilde{\kappa} \left(\sum_\mu \sin^2 q_\mu \right)^2 \right\}, \quad (4.12)$$

where L^4 is the volume of the lattice and $F(q)$ is defined in eq. (3.8). We note that after expanding eq. (4.12) in powers of q and setting $q_\mu = gA_\mu$, we recover to leading order the classical potential in eq. (2.17). In infinite volume, the phases q can be determined from the four saddle-point equations,

$$\left[2(16\tilde{\kappa} + \kappa) - 8\tilde{\kappa} F(q) - 4\tilde{\kappa} \left(\sum_\mu \sin^2 q_\mu \right) \cos q_\nu \right] \sin q_\nu = 0. \quad (4.13)$$

In finite volume, the value of q that minimizes $S_0(q; \tilde{\kappa}, \kappa)$ at a given $(\tilde{\kappa}, \kappa)$ point in the FMD phase is determined by computing $S_0(q; \tilde{\kappa}, \kappa)$ for all L^4 vectors q numerically, and picking out the ones with the smallest value of $S_0(q; \tilde{\kappa}, \kappa)$. (The minimum will respect the lattice symmetries and hence will in general not be unique.) From the resulting q -values we have computed the observable $F(q)$, cf. eq. (3.8), for several $(\tilde{\kappa}, \kappa)$ points in the FMD phase. The discussion of this quantity will be postponed to Sect. 5.2 where we will compare it with the results of the numerical simulation.

We will from now on focus on the physics in the FM phase where $q = 0$, and calculate the magnetization to one higher order in perturbation theory. From this calculation we will obtain another estimate for the critical coupling $\kappa_{\text{FM-FMD}}(\tilde{\kappa})$.

The vertex function $\mathcal{V}_0(k_1, k_2, k_3, k_4)$ in eq. (4.2) is given by

$$\begin{aligned} \mathcal{V}_0(k_1, k_2, k_3, k_4) = & -\frac{1}{4\tilde{\kappa}} \left\{ - \left[\sum_{\mu} (1 - \cos(k_1 + k_2)_{\mu}) \right]^2 + \frac{4}{3} \left[\sum_{\mu} (1 - \cos k_{1\mu}) \right]^2 \right. \\ & + \sum_{\mu\nu} \sin k_{1\mu} \sin k_{2\mu} \sin k_{3\nu} \sin k_{4\nu} + \frac{1}{2} m^2 \sum_{\mu} (1 - \cos(k_1 + k_2)_{\mu}) \\ & \left. - \frac{2}{3} m^2 \sum_{\mu} (1 - \cos k_{1\mu}) \right\} \delta(k_1 + k_2 + k_3 + k_4), \end{aligned} \quad (4.14)$$

where the first three terms arise from the $\tilde{\kappa} \sum_x \{ \phi_x^{\dagger} (\square^2 \phi)_x - B_x^2 \}$ term and the two terms proportional m^2 from the $-\kappa \sum_x \phi_x^{\dagger} (\square \phi)_x$ term in the action (2.24). We note that the vertex function (4.14) can be easily rewritten such that it is symmetric with respect to the momenta k_1, k_2, k_3 and k_4 . For the perturbative calculation it does not matter which form is used.

After carrying out the higher-order calculation, the magnetization can be written in the form

$$v = \exp \left(-\frac{1}{4\tilde{\kappa}} \int_k \Delta_{0,1\text{-loop}}(k) \right) + \text{higher order corrections}, \quad (4.15)$$

$$\Delta_{0,1\text{-loop}}(k) = \frac{\Delta_0(k)}{1 + \Delta_0(k)\Sigma(k)} = \frac{1}{\Delta_0^{-1}(k) + \Sigma(k)} \quad (4.16)$$

where $\Delta_0(k)$ is the tree-level propagator in the FM phase (cf. eq. (4.4) with $q = 0$) and $\Sigma(k)$ is the self-energy,

$$\begin{aligned} \Sigma(k) = & \frac{1}{\tilde{\kappa}} \int_p \left\{ 2 \left[\sum_{\mu} (1 - \cos(p + k)_{\mu}) \right]^2 \right. \\ & \left. - 2 \left(\left[\sum_{\mu} (1 - \cos k_{\mu}) \right]^2 + \left[\sum_{\mu} (1 - \cos p_{\mu}) \right]^2 \right) \right\} \end{aligned}$$

$$\begin{aligned}
& - \sum_{\mu} \sin^2 k_{\mu} \sum_{\nu} \sin^2 p_{\nu} - 2 \left(\sum_{\mu} \sin k_{\mu} \sin p_{\mu} \right)^2 \\
& + m^2 \left(\sum_{\mu} (1 - \cos(p+k)_{\mu}) - \sum_{\mu} (1 - \cos k_{\mu}) - \sum_{\mu} (1 - \cos p_{\mu}) \right) \Big\} \Delta_0(p) .
\end{aligned} \tag{4.17}$$

The propagator (4.16) already involves a resummation of diagrams shown in fig. 2b. The magnetization in eq. (4.15) has been obtained by performing the resummation of diagrams in fig. 2a, but now using the propagator $\Delta_{0,1\text{-loop}}(k)$ instead of $\Delta_q(k)$. In order to compare the perturbative formulas (4.8) and (4.15) with the results of the numerical simulations (see Sect. 5.2) we have to evaluate the lattice integrals in eqs. (4.8) and (4.15) on a finite lattice. The integrals are replaced by sums over the lattice momenta. In this context we note that these finite lattice sums do not include the zero mode, $k = 0$. The zero mode decouples from the action, and gives rise to a phase which disappears after taking the modulus in the definition of v and v_H in eqs. (2.29) and (2.31).

The critical coupling can be calculated by expanding $\Delta_{0,1\text{-loop}}(k)^{-1}$ for small momenta in powers of k^2 ,

$$\Delta_{0,1\text{-loop}}(k)^{-1} = \Delta_0(k)^{-1} + \Sigma(k) = a(\tilde{\kappa}, \kappa) (k^2) + b(\tilde{\kappa}, \kappa) (k^2)^2 + \dots \tag{4.18}$$

and equating the coefficient $a(\tilde{\kappa}, \kappa)$ to zero,

$$\begin{aligned}
a(\tilde{\kappa}, \kappa) &= \frac{\kappa}{\tilde{\kappa}} + \frac{1}{\tilde{\kappa}} \int_k \left\{ \frac{1}{2} \sum_{\mu} (1 - \cos k_{\mu}) \sum_{\nu} \cos k_{\nu} - \sum_{\mu} \sin^2 k_{\mu} \right. \\
&\quad \left. + \frac{\kappa}{\tilde{\kappa}} \left(\frac{1}{8} \sum_{\mu} \cos^2 k_{\mu} - \frac{1}{2} \right) \right\} \Delta_0(k) = 0 .
\end{aligned} \tag{4.19}$$

This leads to the one-loop estimate

$$\begin{aligned}
\kappa_{\text{FM-FMD}}(\tilde{\kappa}) &= - \int_k \left\{ \frac{1}{2} \sum_{\mu} (1 - \cos k_{\mu}) \sum_{\nu} \cos k_{\nu} - \sum_{\mu} \sin^2 k_{\mu} \right\} \\
&\quad \times \left[\sum_{\mu} (1 - \cos k_{\mu}) \right]^{-2}
\end{aligned} \tag{4.20}$$

$$\approx 0.02993 , \tag{4.21}$$

which is about a factor two larger than the mean-field value, cf. table 1.

5 Numerical Results

5.1 Phase Diagram

To simulate the reduced model defined by the path integral (2.23) we have implemented two different Monte Carlo algorithms, a five-hit Metropolis and a Hybrid Monte Carlo algorithm. The results for the various observables agree nicely within the AM, FM and PM phases. We find however that the Hybrid Monte Carlo algorithm gets much more easily stuck in metastable non-equilibrium states in the FMD phase. We therefore have generated the bulk of the data presented in this paper with a five-hit Metropolis algorithm.

To map the phase diagram we have measured the following observables:

- The *magnetization*

$$v = \left\langle \left| \frac{1}{L^4} \sum_x \phi_x \right| \right\rangle , \quad (5.1)$$

which is the order parameter for ferromagnetism and

- the *staggered magnetization*

$$v_{\text{AM}} = \left\langle \left| \frac{1}{L^4} \sum_x \phi_x \epsilon_x \right| \right\rangle , \quad (5.2)$$

which is the order parameter for anti-ferromagnetism.

- The *helicoidal magnetization*

$$v_{\text{H}} = \left\langle \left| \frac{1}{L^4} \sum_x \phi_x \exp \left(-i \sum_{\mu} q_{\mu} x_{\mu} \right) \right| \right\rangle \quad (5.3)$$

was used to map the FMD phase, where the four real phases q_{μ} , $\mu = 1, \dots, 4$ were determined for each configuration from

$$q_{\mu} = \text{Im Log} \left[\frac{1}{L^4} \sum_x \phi_x^{\dagger} \phi_{x+\hat{\mu}} \right] . \quad (5.4)$$

- Apart from these quantities we have also measured the internal energy density

$$z^2 = \left\langle \frac{1}{4L^4} \sum_{\mu x} \text{Re} \left(\phi_x^{\dagger} \phi_{x+\hat{\mu}} \right) \right\rangle \quad (5.5)$$

of the mass counterterm and

- the quantity

$$c(q_{\mu}) = \langle \cos q_{\mu} \rangle , \quad (5.6)$$

where the phases q_{μ} were calculated for each configuration by means eq. (5.4).

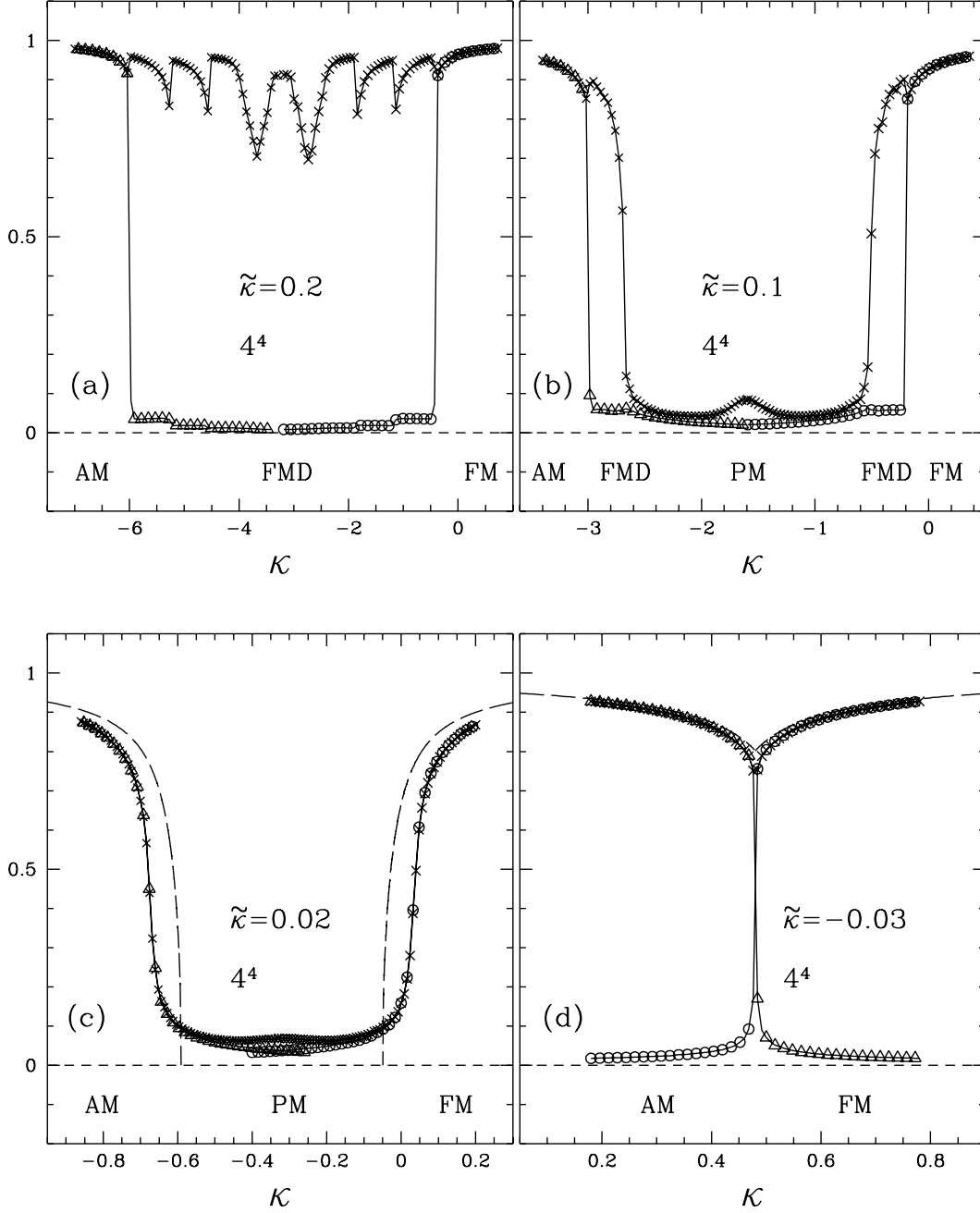


Figure 3: Scans in κ direction on a 4^4 lattice at $\tilde{\kappa} = 0.2$ (fig. a) $\tilde{\kappa} = 0.1$ (fig. b) $\tilde{\kappa} = 0.02$ (fig. c) and $\tilde{\kappa} = -0.03$ (fig. d). The results for v , v_{AM} and v_H are represented in the plots by the circles, triangles and crosses. The error bars are omitted because they are in all cases smaller than the symbol size. The dashed lines in figs. c and d are obtained in the mean-field approximation.

We have taken the modulus in eqs. (5.1-5.3) for each configuration, because, in a finite volume, the constant field mode gives rise to a slow drift of the magnetization through the group space. (Taking the absolute value is a standard method which allows us to avoid the introduction of an external magnetic field.)

The discreteness of the phases (4.11) poses a problem for the simulation in the FMD phase because each transition of one q to another q behaves very much like a first order phase transition and hence is accompanied by metastabilities. We find that these metastabilities become more severe when the lattice size is increased.

To determine the phase diagram we kept the parameter $\tilde{\kappa}$ fixed and performed simulations at a large number of κ values. Each of these vertical scans, cf. fig. 1, has been started in the FM phase. We lowered κ in fixed steps and used the last configuration of a run as the initial configuration at the next smaller value of κ . At each point we skipped 10^3 sweeps for equilibration and performed 10^4 measurement sweeps. The error of an observable O was determined using the relation

$$\Delta\langle O \rangle = \Delta\langle O \rangle_{\text{st}} \sqrt{2\tau_{\text{int}}} , \quad (5.7)$$

where $\Delta\langle O \rangle_{\text{st}}$ is the standard deviation and τ_{int} designates the integrated autocorrelation time, defined as $\tau_{\text{int}} = \sum_{\Delta t} \Gamma(\Delta t) / \Gamma(0)$ (see for example [22]). The quantity $\Gamma(\Delta t) = \langle O(t)O(t + \Delta t) \rangle - \langle O \rangle^2$ is the autocorrelation function.

In figs. 3a-d we have displayed the numerical results for the order parameters v (circles), v_{AM} (triangles) and v_{H} (crosses) for four exemplary scans on a 4^4 lattice. Fig. 3a shows that there are three different phases at $\tilde{\kappa} = 0.2$, an FM phase at $\kappa \gtrsim -0.43$, where $v = v_{\text{H}} > 0$, $v_{\text{AM}} = 0$, an AM phase at $\kappa \lesssim -5.97$, where $v_{\text{AM}} = v_{\text{H}} > 0$, $v = 0$ and the FMD phase at intermediate κ in which $v_{\text{H}} > 0$, $v = v_{\text{AM}} = 0$. The helicoidal magnetization v_{H} exhibits jumps at certain κ values within the FMD phase. These jumps in v_{H} occur because the phases q_{μ} can change only in discrete steps and hence have to be considered as a finite volume artifact. In Fig. 4a we have plotted the quantity $c(q_{\mu})$, $\mu = 1, \dots, 4$ for the same scan at $\tilde{\kappa} = 0.2$ as a function of κ . A comparison of figs. 3a and 4a shows that the jumps in v_{H} occur at the same κ values where one of the components $c(q_{\mu})$ exhibits a jump. All q_{μ} 's are zero in the FM phase. At $\kappa \approx -0.43$ the first component of q condenses (dotted line) and becomes equal to $2\pi/L = \pi/2$. The next jump occurs when also the second component of q becomes equal to $\pi/2$ (solid line). The κ value where finally all values of q are equal to $\pi/2$ coincides nicely with the symmetry point, $\kappa = -16\tilde{\kappa} = -3.2$, cf. eq. (3.18). We note that the order in which the jumps occur is arbitrary (because of hypercubic symmetry). The jumps at $\kappa < -16\tilde{\kappa}$ follow a similar pattern, with the q_{μ} 's jumping from $\pi/2$ to π . We will show in Sect. 5.2 that the complicated κ -dependence of v_{H} in the FMD phase can at least qualitatively be explained by the one-loop formula (4.8). In fig. 4b we have plotted the internal energy density z^2 as a function of κ . In the mean-field theory this quantity is given

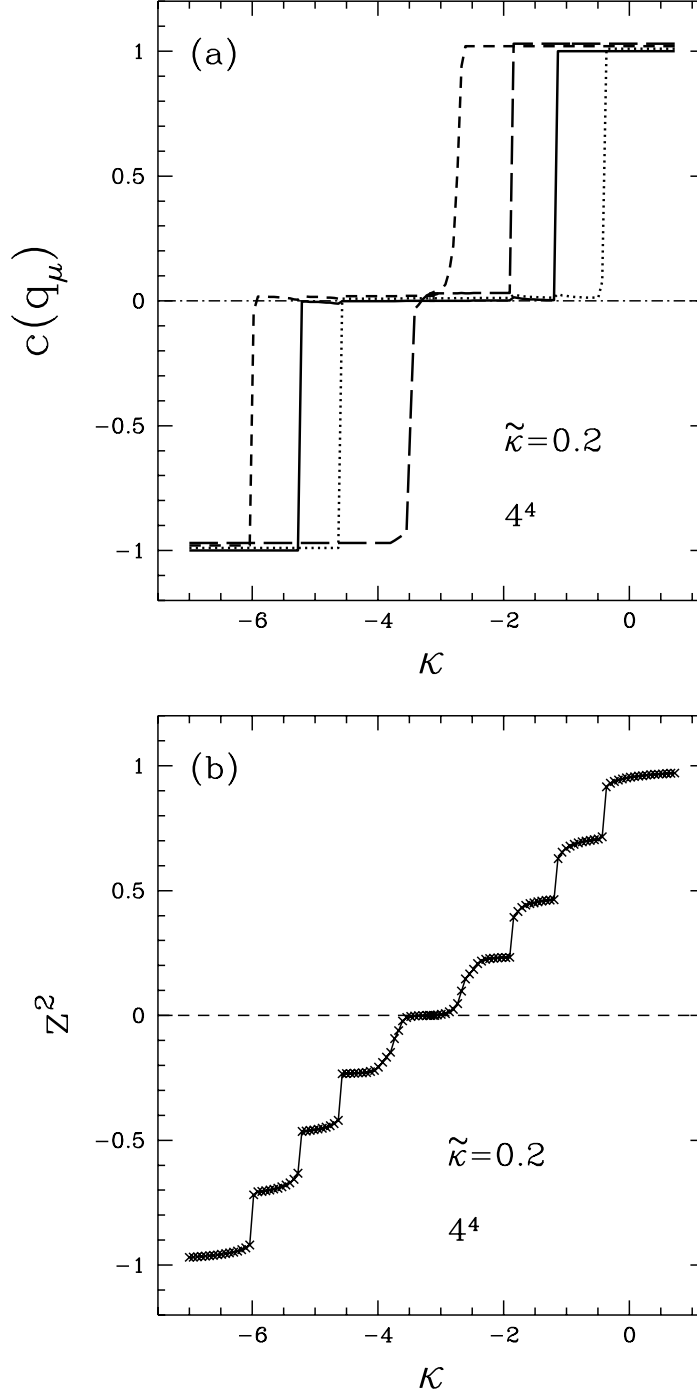


Figure 4: The observables $c(q_\mu)$ (fig. a) and z^2 (fig. b) as a function of κ for $\tilde{\kappa} = 0.2$. The lattice size is 4^4 . The four observables $c(q_\mu)$, $\mu = 1, \dots, 4$ are distinguished by the line type (solid, dots, long and short dashes). The error bars are omitted in both figures because they are not larger than the symbol size in fig. b and also not much bigger than the line width in fig. a.

by $v_H^2 \frac{1}{4} \sum_{\mu} \cos q_{\mu}$ and since $v_H^2 = O(1)$, we expect this quantity to jump whenever q changes. The comparison of figs. 4a and 4b shows that this is indeed the case.

A different situation is encountered in fig. 3b which shows the result of the scan at $\tilde{\kappa} = 0.1$. Besides the FM, AM and FMD phases we find now clear evidence for a PM phase (where $v = v_{AM} = v_H = 0$) which, as predicted by the mean-field calculation, extends into the FMD phase. The graph shows that four different phase boundaries are crossed when κ is lowered from the FM to the AM phase. The small peak at $\kappa = -16\tilde{\kappa} \approx -1.6$ appears to be a finite size effect because it becomes smaller when the lattice size is enlarged.

The FMD phase gradually disappears when $\tilde{\kappa}$ is lowered further. The situation at $\tilde{\kappa} = 0.02$ is depicted in fig. 3c. The FMD phase has now completely disappeared, and the only three phases we are left with are the FM, PM and AM phases. We find that the PM phase extends down to $\tilde{\kappa} \approx -0.02$. The result of the scan at $\tilde{\kappa} = -0.03$ is displayed in fig. 3d. It shows that the phase transition between the FM and AM phase coincides with the symmetry line $\kappa = -16\tilde{\kappa}$ and is obviously of first order. Both the internal energy density z^2 and the order parameters v and v_{AM} exhibit a gap at this phase transition. This gap grows from zero to one when one follows the symmetry line $\kappa = -16\tilde{\kappa}$ from the triple point where the FM, PM and AM phases meet to $\tilde{\kappa} = -\infty$. The two dashed lines in figs. 3c and d represent the mean-field result for the magnetization $\varphi = v$ in the FM and for the staggered magnetization $\varphi = v_{AM}$ in the AM phase, which we obtained by solving the mean-field equations (3.10) and (3.12) for $q = (0, 0, 0, 0)$ and $q = (\pi, \pi, \pi, \pi)$ numerically.

We have read off the positions of the various phase transitions from plots like the ones depicted in figs. 3a-d and then compiled them in the κ - $\tilde{\kappa}$ phase diagram plot in fig. 1. The triangles were obtained on a 4^4 lattice, the crosses represent the phase boundaries on a 6^4 lattice and the circles mark the phase transitions points on an 8^4 lattice. The solid curves are the mean-field results which we discussed in Sect. 3. The plot shows that the numerical estimates for the FM-AM, FM-PM, PM-AM, FM-FMD and FMD-AM phase boundaries agree nicely with the mean-field prediction. The agreement seems to be worse for the FMD-PM phase transition. The numerical data indicate however that both the horizontal and vertical width of the PM phase shrink when the lattice size is increased and that the numerical results could come out closer to the mean-field result for larger volumes.

In fig. 5 we have displayed the magnetization v as a function of κ for $\tilde{\kappa} = 0.2$ and a series of different lattice sizes. Again, we have lowered κ in small steps, and used the last configuration of a run as initial configuration for the next run, skipping 10^3 sweeps for equilibration.

First we discuss the results on the smaller lattices of size 3^4 (filled circle), 4^4 (filled square) and 5^4 (filled triangles). The magnetization v exhibits a jump on these lattices. The helicoidal magnetization v_H is identical with v in the FM phase

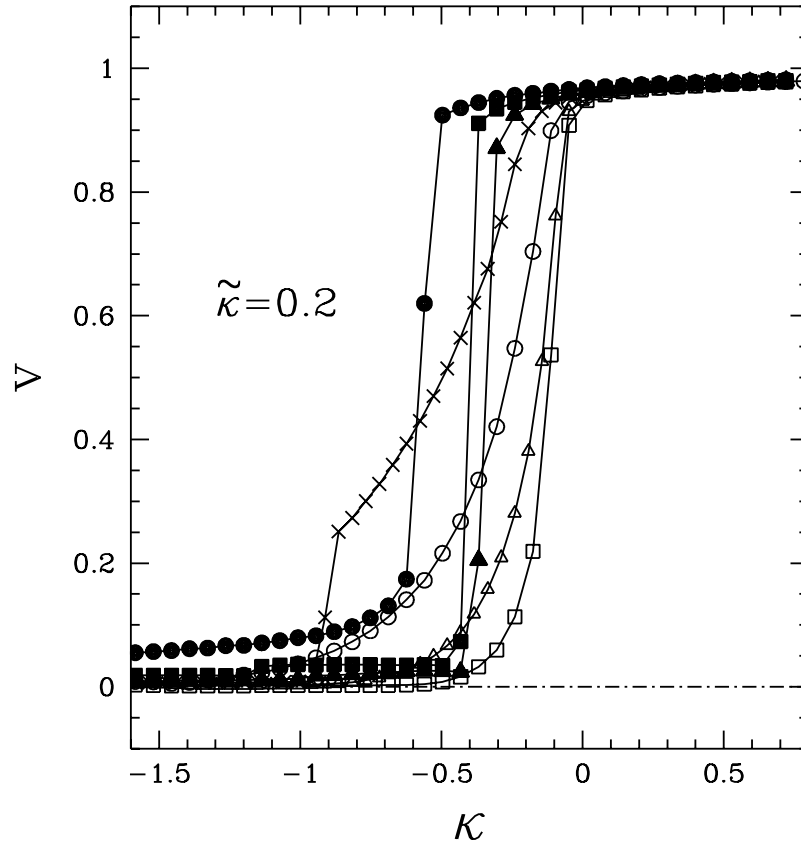


Figure 5: The magnetization v as a function of κ at $\tilde{\kappa} = 0.2$ on 3^4 (filled circle), 4^4 (filled square), 5^4 (filled triangle), 6^4 (crosses), 8^4 (open circle), 10^4 (open triangle) and 12^4 (open square) lattices.

and (unlike v) remains of $O(1)$ when crossing the FM-FMD phase transition towards the FMD phase (the data for v_H are not included in fig. 5). It can be seen that the curves for v bend in more strongly when the lattice size is increased, indicating that v scales to zero at the FM-FMD phase transition as predicted by the weak coupling expansion in Sect. 4. We will demonstrate in the next subsection that the data for v in the FM phase are nicely consistent with the perturbative formula (4.15) according to which $v \searrow 0$ in the limit $\kappa \searrow \kappa_{\text{FM-FMD}}$ and $L \rightarrow \infty$. The plot also shows that $\kappa_{\text{FM-FMD}}$ increases with increasing lattice size.

On the larger lattices we encounter a different behavior. The magnetization first starts to bend over when κ is lowered but then instead of jumping to the FMD phase continues to decrease slowly. The jump to the FMD occurs finally at a large negative value of κ . The jump on the 6^4 lattice (crosses) for instance occurs at $\kappa \approx -0.9$ and not at $\kappa \approx -0.2$. The reason for this effect could be related to the fact that the FM-FMD phase transition behaves very much like a first order phase transition as the magnetization drops to zero very rapidly at $\kappa_{\text{FM-FMD}}$. On the larger lattices the fluctuations in the internal energy are very small and hence the probability for a jump across a large energy barrier becomes strongly suppressed. This situation did not change after increasing the statistics by one order of magnitude which means that the probability for a transition to occur at larger κ is very small. In this context we also note that on larger lattices the system in the FMD phase ends up in different states when using different starting configurations and transitions to other states occur very rarely or not at all. The results for the various observables in the FMD phase are independent of the initial configuration only on the smaller lattices of size 3^4 , 4^4 and 5^4 . (In all other phases, our results are independent of the initial configurations on all volumes.)

Fig. 5 shows that the region in the FM phase where the magnetization starts to bend over is shifted in all cases towards larger values of κ when the lattice size is enlarged. We will show in the next subsection that this finite size behavior is in nice agreement with the perturbative formula given in Sect. 4. This good agreement between the numerical data and lattice perturbation theory lead us to identify $\kappa_{\text{FM-FMD}}$ on the larger lattices, i.e. for $L \geq 6$, with the point where the slope in v is largest, and not with the point at large negative κ , where v exhibits the jump and v_H becomes different from v . All phase transition points on the 6^4 and 8^4 lattice which are included in fig. 1 were obtained with this criterion.

5.2 Comparison with Perturbation Theory

In this subsection we compare the simulation results for v in the FM and v_H in the FMD phase with the perturbative formulas which we derived in Sect. 4. In fig. 6 we have plotted once more the v and v_H data of fig. 3a which were obtained at $\tilde{\kappa} = 0.2$

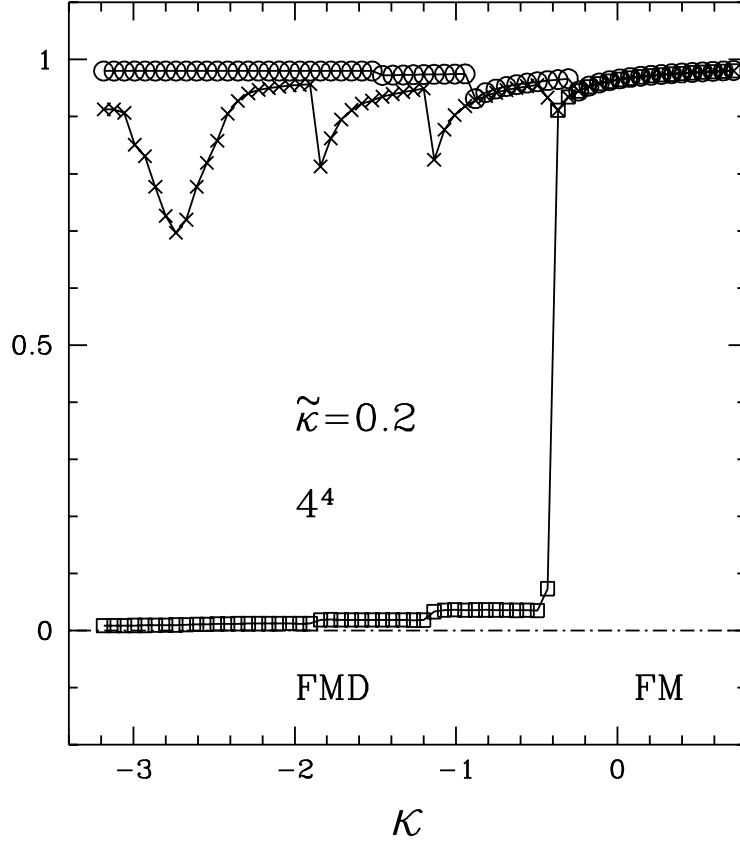


Figure 6: The magnetization v (squares) and the helicoidal magnetization v_H (crosses) in the FM and FMD phases as a function of κ for $\tilde{\kappa} = 0.2$. The same data were presented already in fig. 3a. The circles were obtained by numerically evaluating the perturbative expression (4.8). The phases $q_\mu = q_\mu(\tilde{\kappa}, \kappa)$ were obtained by minimizing eq. (4.12).

on a 4^4 lattice. The circles in fig. 6 were obtained by evaluating the one-loop formula for v_H (4.8) numerically on both sides of the FM-FMD phase transition on the same lattice and at the same values of κ where we performed the numerical simulations. The phases $q(\tilde{\kappa}, \kappa)$ at a given value of κ were determined analytically by minimizing the classical action in eq. (4.12) with $L = 4$. Fig. 6 shows that the numerical results are nicely reproduced by the analytic formula (4.8) at large values of κ . At smaller κ values the deviations start to become larger. While we do not understand this phenomenon in detail, we believe that it may be related to the metastabilities mentioned in Sect. 5.1. (Higher orders in perturbation theory could also be sizable though.) The jumps at which the components of q condense occur slightly delayed. This distorts the κ -dependence of the propagator, which depends also explicitly on κ and not only implicitly through the phases $q(\tilde{\kappa}, \kappa)$. From the minimizing phases $q(\tilde{\kappa}, \kappa)$ on the 4^4 lattice we have computed the function $F(q)$, cf. eq. (3.8), which we plotted in fig. 7a (dashed line) versus κ . The numerical results for z^2 , which in the mean-field approximation are proportional to $F(q)$ are represented in this graph by the crosses. It can be seen that the gap between the two curves widens up when κ is lowered, which is presumably due to the systematic delay of the transition events in the numerical simulation. We should observe a smaller shift on a smaller lattice if this scenario is correct. Fig. 7b shows that the gap between the two curves shrinks indeed on the 3^4 lattice. We also checked that the numerical metastabilities on a 5^4 lattice get stronger making the agreement with the analytic results worse. Note that the discrepancies between perturbation theory and numerical data occur at the same locations in figs. 6 and 7a.

In the following we will discuss only the FM phase. The numerical metastabilities mentioned in the previous paragraph have an effect on the simulation results only in the near vicinity of the FM-FMD phase transition.

In fig. 8 the magnetization v for $\tilde{\kappa} = 0.1$ is displayed as a function of κ . The lattice size is 8^4 . At each κ point we have accumulated a statistics of 10^5 Metropolis sweeps. The magnetization was measured after each sweep and its error was computed by means of eq. (5.7). To compare the numerical data with the perturbative formulas, we have numerically evaluated the integrals (replaced by lattice sums) in eq. (4.8) and (4.15) for a large number of κ values in the FM phase on the same lattice which we used in the numerical simulations. The obtained results for v in eqs. (4.8) and (4.15) are represented by the dashed and solid curves. Fig. 8 shows that the two-loop formula (4.15) provides, as expected, a much better description of the numerical data than the one-loop formula (4.8). The fact that perturbation theory in $1/\tilde{\kappa}$ remains valid down to such small values of $\tilde{\kappa}$ is because the actual expansion parameter is not $1/\tilde{\kappa}$ but $1/(16\pi^2\tilde{\kappa})$ where the factor $1/(16\pi^2)$ comes from the loop integrals.

The $\tilde{\kappa}$ -dependence of the magnetization v is shown in fig. 9, where we have plotted the magnetization data for five different $\tilde{\kappa}$ values versus κ . The lattice size

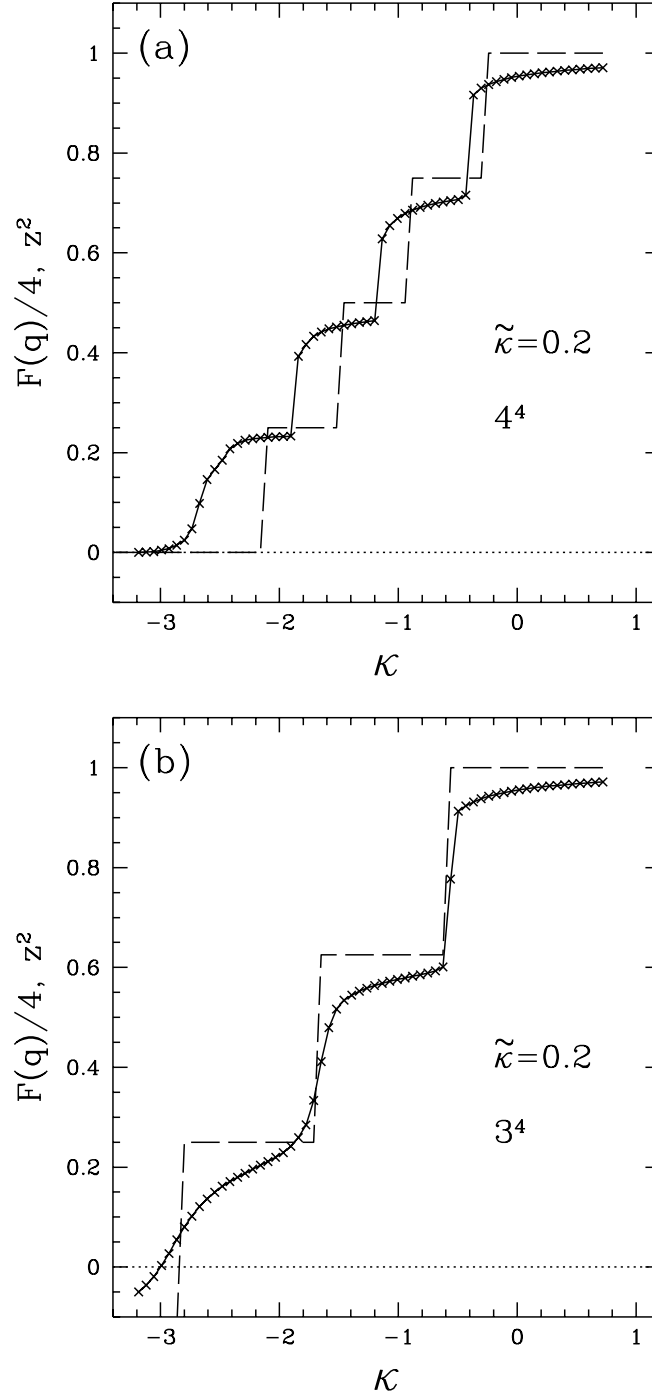


Figure 7: The quantity $\frac{1}{4}F(q)$ (dashed line), obtained from the minimization of the classical action (4.12), and the internal energy density z^2 (crosses), obtained from the numerical simulation, as a function of κ for $\tilde{\kappa} = 0.2$ on 4^4 (fig. a) and 3^4 (fig. b) lattices.

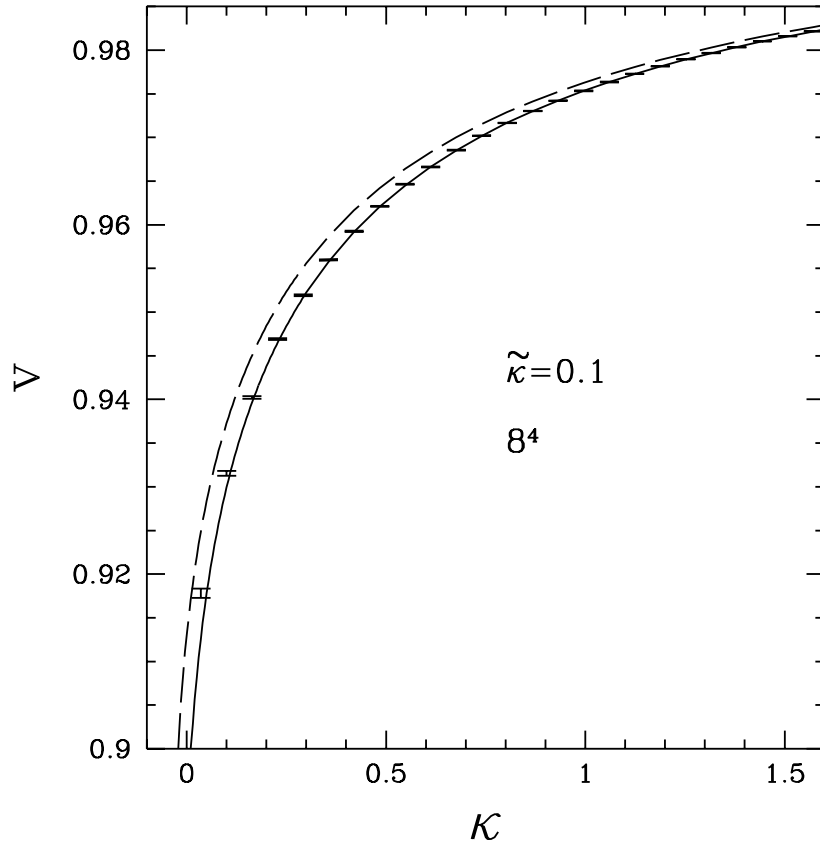


Figure 8: *The magnetization v as a function of κ for $\tilde{\kappa} = 0.1$. The lattice size is 8^4 . The one-loop and two-loop results for v are represented by the dashed, cf. eq. (4.8), and solid, cf. eq. (4.15), curves.*

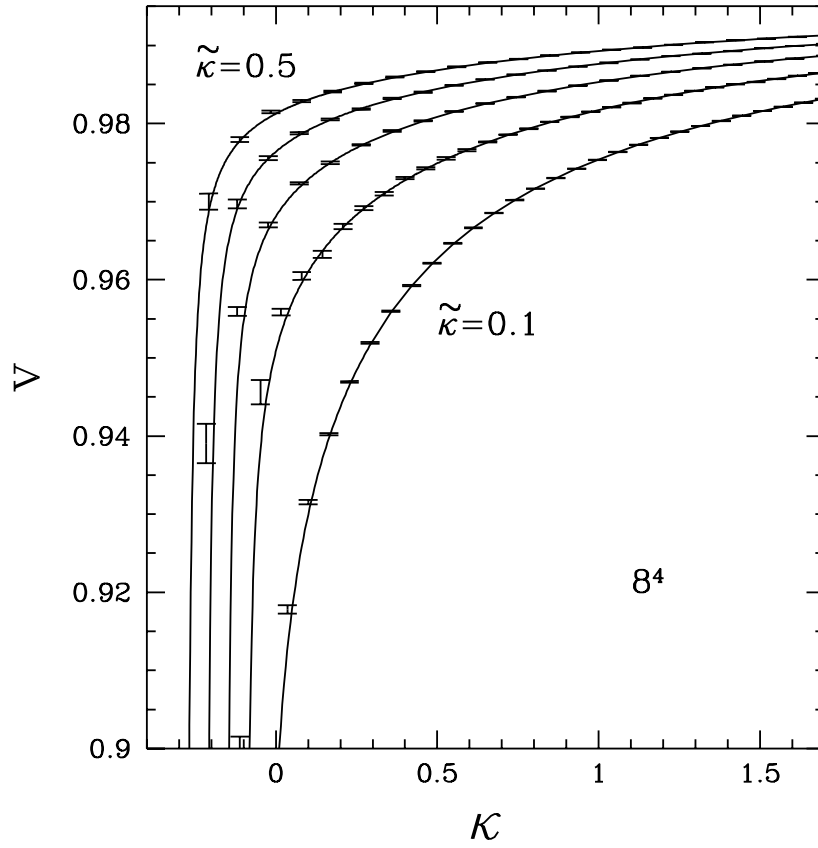


Figure 9: The magnetization v as a function of κ for several values of $\tilde{\kappa}$. The five curves correspond, from the bottom to the top, to $\tilde{\kappa} = 0.1, 0.2, 0.3, 0.4$ and 0.5 . The lattice size is in all cases 8^4 . The solid lines were obtained by evaluating expression (4.15) for a large number of κ values numerically.

is also in this case 8^4 and the statistics at each κ point the same as in fig. 8. In order to better monitor the drop of the magnetization near the FM-FMD phase transition we have increased the density of points in that region. The solid lines represent again the perturbative result according to eq. (4.15). The agreement between the numerical data and the analytic curve is in all cases excellent. The graph shows that the drop to the critical point is becoming steeper when $\tilde{\kappa}$ is increased. This phenomenon is a consequence of the fact that the critical exponent η in eq. (4.10) decreases with increasing $\tilde{\kappa}$.

Finally we demonstrate that also the volume dependence of the magnetization data in the FM phase, cf. fig. 5, is nicely reproduced by the perturbative formula (4.15). In fig. 10 we have plotted v as a function of κ for $\tilde{\kappa} = 0.2$ and five different lattices ranging in size from 3^4 to 8^4 . The statistics at each κ value is about $10^5 \times (8/L)^2$ Metropolis sweeps. The solid lines represent again the perturbative results according to eq. (4.15). The two-loop curve agrees nicely with the numerical data down to the value of κ where the analytic curve has a minimum, but starts to deviate when κ is lowered beyond that value. The two-loop curve increases while the numerical data continue to fall off. This shows that the two-loop formula (4.15) is valid only in the κ interval above the minimum. The self-energy $\Sigma(k)$ in eq. (4.16) diverges at

$$\kappa = \kappa_{\min} = -2 \tilde{\kappa} (1 - \cos 2\pi/L) , \quad (5.8)$$

because the inverse tree-level propagator $\Delta_0^{-1}(k)$ has a zero eigenvalue (for some nonzero k) at this value of κ . This implies that v in eq. (4.15) approaches one in the limit $\kappa \searrow \kappa_{\min}$. (Lowering κ beyond this value would lead to a negative eigenvalue of the tree-level inverse propagator, and this instability causes q to condense to the smallest possible value, cf. eq. (4.11).) The plot shows that the minimum of the two-loop curve gets smaller and also narrower when the size of the lattice is increased. The minimum drops to zero in the infinite volume limit at the κ -value where $a(\tilde{\kappa}, \kappa)$ vanishes, cf. eq. (4.19). This κ -value coincides with the one-loop estimate (4.20) only in the limit $\kappa \rightarrow \infty$. At $\tilde{\kappa} = 0.2$ we find that v drops to zero at $\kappa \approx 0.03446$ which is by about 15% larger than the one-loop estimate in eq. (4.20).

From eq. (5.8) we find that for $\tilde{\kappa} = 0.2$, $\kappa_{\min} = -0.6, -0.4, \approx -0.2764, -0.2$ and -0.1 for $L = 3, 4, 5, 6$ and 8 . Fig. 10 shows that the two-loop curve approaches one at these values of κ .

6 Summary and Outlook

In this paper we have calculated the phase diagram of the *reduced model* for a gauge-fixed U(1) lattice gauge theory in the mean-field approximation. The phase diagram contains a ferromagnetic (FM), anti-ferromagnetic (FM), paramagnetic (PM) and,

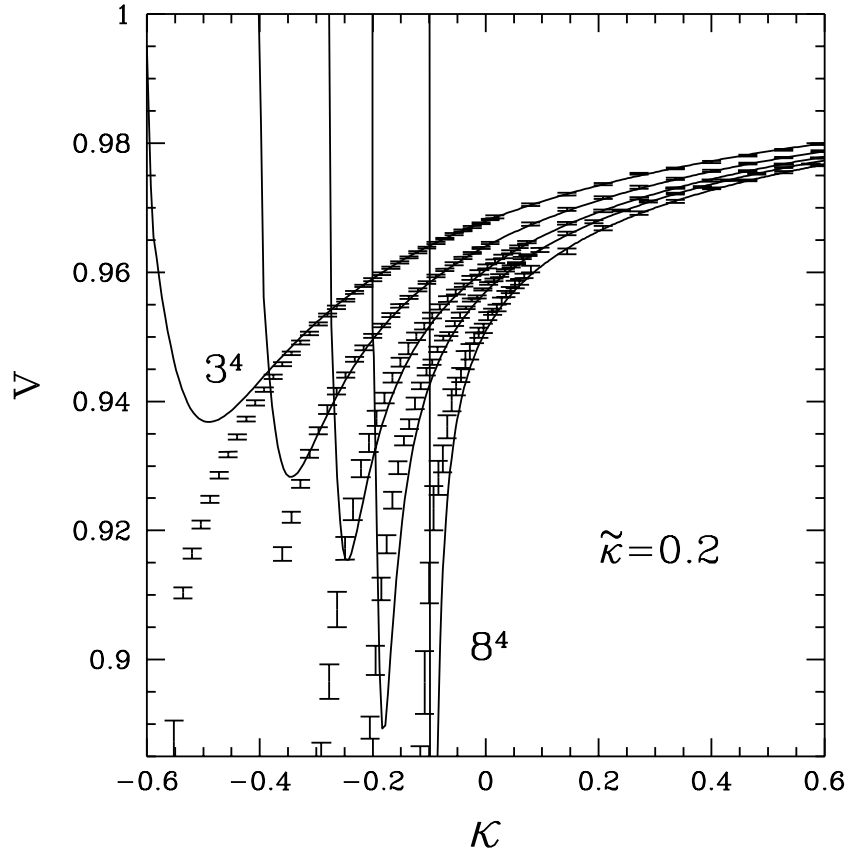


Figure 10: The magnetization v versus κ for $\tilde{\kappa} = 0.2$ and several values of L . The five curves correspond, from the left to the right, to $L = 3, 4, 5, 6$ and 8 . The five solid lines were obtained by computing (4.15) numerically on lattices of the same size.

as a novelty, also a ferromagnetic directional (FMD) phase, where not only the U(1) symmetry is broken but also the vector field condenses. The mean-field results for the phase diagram were confirmed by numerical simulations. The continuum limit of the model corresponds to a continuous phase transition between the FM phase and the FMD phase. We have studied the nature of this phase transition in lattice perturbation theory and demonstrated that the magnetization vanishes in the continuum limit, because of infra-red effects, and that the global U(1) symmetry gets restored in this limit. This phenomenon cannot be understood in the mean-field approximation. We have shown that the numerical data for the magnetization are in good agreement with the results of the weak coupling expansion in the FM phase. We have calculated the critical coupling of the FM-FMD phase transition at large values of $\tilde{\kappa}$ both in the mean-field approximation and in perturbation theory, and find in both cases a small positive value. At $\tilde{\kappa} \rightarrow \infty$ the mean-field result for the FM-FMD phase transition is smaller by about a factor two than the perturbative result.

As a next step we will take up again various proposals for lattice chiral gauge theories and investigate whether the problems associated with the strongly fluctuating gauge degrees of freedom can be overcome by gauge fixing. In refs. [15] and [16] we will show for the case of the reduced abelian Wilson-Yukawa (Smit-Swift) model that a) the species doublers decouple in the continuum limit, and b) that the fermion spectrum contains only the desired states, namely a massless charged left-handed fermion that couples to the gauge field and a massless neutral right-handed fermion that decouples. We expect to find similar positive results also for other fermion formulations, using a Majorana-Wilson term instead of a Dirac-Wilson term [23], domain wall fermions with waveguide [6], or staggered fermions [24].

It is challenging to study the U(1) model with gauge fields turned on. It should be possible to determine the fermion spectrum in the Coulomb phase and see if it remains unaffected at small values of the gauge coupling. A change of the fermion spectrum should manifest itself as a new phase transition in the fermion sector.

It is also important to extend the gauge-fixing approach to nonabelian gauge theories. This implies that we first have to specify how to discretize and simulate the ghost part of the action (2.1). The nonabelian case is very interesting because in this case we can ask whether confinement emerges at small values of the gauge coupling.

Acknowledgements

We thank M. Ogilvie for discussions. W.B. is supported by the Deutsche Forschungsgemeinschaft (DFG). M.G. is supported by the US Department of Energy as an Outstanding Junior Investigator, and Y.S. is supported in part by the US-Israel

Binational Science Foundation, and the Israel Academy of Science. The numerical calculations were performed on the SP2 at DESY-IfH Zeuthen and numerous workstations and PCs at the Physics Departments of Washington University, St. Louis, and Humboldt University, Berlin. Some of the first explorative calculations were performed on the HP-cluster of the Center for Computational Physics of the University of Tsukuba. W.B. thanks Washington University, St. Louis for hospitality and M.G. thanks the Center for Computational Physics of the University of Tsukuba, the Benasque Center for Physics and Humboldt University, Berlin, for hospitality.

References

- [1] K. Wilson, in *New Phenomena in Sub-Nuclear Physics* (Erice, 1975), ed. A. Zichichi (Plenum New York, 1977)
- [2] J. Smit, *Acta Physica Polonica* B17 (1986) 531 (Zakopane 1985);
L.H. Karsten, in *Field Theoretical Methods in Particle Physics*, ed. W. Rühl, Plenum (1980) (Kaiserslautern 1979);
J. Smit, *Nucl. Phys.* B175 (1980) 307
- [3] P.D.V. Swift, *Phys. Lett.* B145 (1984) 256
- [4] D. Foerster, H.B. Nielsen and M. Ninomiya, *Phys. Lett.* B94 (1980) 135;
J. Smit, *Nucl. Phys. B (Proc.Suppl.)* 4 (1988) 451;
S. Aoki, *Phys. Rev. Lett.* 60 (1988) 2109;
K. Funakubo and T. Kashiwa, *Phys. Rev. Lett.* 60 (1988) 2113
- [5] E. Eichten, J. Preskill, *Nucl. Phys.* B268 (1986) 179;
M.F.L. Golterman, D.N. Petcher, E. Rivas, *Nucl. Phys.* B395 (1993) 596;
Nucl. Phys. B (Proc.Suppl.) 26 (1992) 486
- [6] D.B. Kaplan, *Nucl. Phys. B (Proc.Suppl.)* 30 (1992) 597;
M.F.L. Golterman, K. Jansen, D.N. Petcher, J.C. Vink, *Phys. Rev.* D49 (1994) 1606;
M.F.L. Golterman, Y. Shamir, *Phys. Rev.* D51 (1995) 3026
- [7] M.F.L. Golterman, D.N. Petcher, J. Smit, *Nucl. Phys.* B370 (1992) 51;
W. Bock, A.K. De and J. Smit, *Nucl. Phys.* B388 (1992) 243;
M.F.L. Golterman, D.N. Petcher, E. Rivas, *Nucl. Phys.* B377 (1992) 405
- [8] Y. Shamir, *Phys. Rev. Lett.* 71 (1993) 2691; *Nucl. Phys. B (Proc.Suppl.)* 34 (1994) 590; hep-lat/9307002

- [9] Y. Shamir, Nucl. Phys. B (Proc. Suppl.) 47 (1996) 212
- [10] D.N. Petcher, Nucl. Phys. B (Proc. Suppl.) 30 (1993) 50
- [11] Y. Shamir, TAUP-2306-95 (hep-lat/9512019); Nucl. Phys. B (Proc. Suppl.) 53 (1997) 664
- [12] A. Borelli, L. Maiani, G.-C. Rossi, R. Sisto, M. Testa, Phys. Lett. B221 (1989) 360; Nucl. Phys. B333 (1990) 335
- [13] M.F.L. Golterman, Y. Shamir, Phys. Lett. B399 (1997) 148
- [14] K. Jansen, J. Kuti, and C. Liu, Phys. Lett. B309 (1993) 119; Nucl. Phys. B (Proc. Suppl.) 30 (1993) 681; B34 (1994) 635; B42 (1995) 630; J. Kuti, Nucl. Phys. B (Proc. Suppl.) 42 (1995) 113
- [15] W. Bock, M.F.L. Golterman, Y. Shamir, in preparation
- [16] W. Bock, M.F.L. Golterman, Y. Shamir, in preparation
- [17] H. Neuberger, Phys. Lett. B183 (1987) 337
- [18] B. Sharpe, Jour. Math. Phys. 25 (1984) 3324
- [19] W. Selke, Spatially modulated structures in systems with competing interactions, in *Phase Transitions and Critical Phenomena*, Vol. 15, eds. C. Domb and J.L. Lebowitz, Academic Press, 1992, pg. 1
- [20] J. Zinn-Justin, *Quantum Field Theory and Critical Phenomena*, Third Edition, 1996, Oxford University Press, chapter 24
- [21] N.D. Mermin and H. Wagner, Phys. Rev. Lett. 17 (1966) 1133; S. Coleman, Comm. Math. Phys. 31 (1973) 259; S. Elitzur, Nucl. Phys. B212 (1983) 501; F. David, Phys. Lett. B96 (1980) 371, Comm. Math. Phys. 81 (1981) 149; Nucl. Phys. B190 (1981) 205
- [22] A. Sokal, Nucl. Phys. B (Proc. Suppl.) 20 (1991) 55
- [23] C. Pryor, Phys. Rev. D43 (1991) 2669; L. Maiani, G.-C. Rossi, M. Testa, Phys. Lett. B292 (1992) 397
- [24] J. Smit, Nucl. Phys. B (Proc. Suppl.) 26 (1992) 480; Nucl. Phys. (Proc. Suppl.) 29B,C (1992) 83; W. Bock, J. Smit, J.C. Vink, Nucl. Phys. B414 (1994) 73; B416 (1994) 645